

## A Marchenko equation for acoustic inverse source problems

Joost van der Neut, Jami L. Johnson, Kasper van Wijk, Satyan Singh, Evert Slob, and Kees Wapenaar

Citation: *The Journal of the Acoustical Society of America* **141**, 4332 (2017); doi: 10.1121/1.4984272

View online: <http://dx.doi.org/10.1121/1.4984272>

View Table of Contents: <http://asa.scitation.org/toc/jas/141/6>

Published by the *Acoustical Society of America*

---

---

# A Marchenko equation for acoustic inverse source problems

Joost van der Neut,<sup>1,a)</sup> Jami L. Johnson,<sup>2</sup> Kasper van Wijk,<sup>2</sup> Satyan Singh,<sup>3</sup> Evert Slob,<sup>1</sup> and Kees Wapenaar<sup>1</sup>

<sup>1</sup>*Department of Geoscience and Engineering, Delft University of Technology, 2600 GA Delft, the Netherlands*

<sup>2</sup>*Dodd-Walls Centre for Photonic and Quantum Technologies, Department of Physics, University of Auckland, Auckland 1010, New Zealand*

<sup>3</sup>*School of Geosciences, The University of Edinburgh, Edinburgh EH9 3FE, United Kingdom*

(Received 29 December 2016; revised 4 April 2017; accepted 14 May 2017; published online 12 June 2017)

From acoustics to medical imaging and seismology, one strives to make inferences about the structure of complex media from acoustic wave observations. This study proposes a solution that is derived from the multidimensional Marchenko equation, to learn about the acoustic source distribution inside a volume, given a set of observations outside the volume. Traditionally, this problem has been solved by backpropagation of the recorded signals. However, to achieve accurate results through backpropagation, a detailed model of the medium should be known and observations should be collected along a boundary that completely encloses the volume of excitation. In practice, these requirements are often not fulfilled and artifacts can emerge, especially in the presence of strong contrasts in the medium. On the contrary, the proposed methodology can be applied with a single observation boundary only, without the need of a detailed model. In order to achieve this, additional multi-offset ultrasound reflection data must be acquired at the observation boundary. The methodology is illustrated with one-dimensional synthetics of a photoacoustic imaging experiment. A distribution of simultaneously acting sources is recovered in the presence of sharp density perturbations both below and above the embedded sources, which result in significant scattering that complicates the use of conventional methods. © 2017 Acoustical Society of America.

[<http://dx.doi.org/10.1121/1.4984272>]

[JFL]

Pages: 4332–4346

## I. INTRODUCTION

A common problem in acoustics is to image the wavefield from a distribution of sources, given a set of observations. We refer to this problem as the Inverse Source Problem (ISP). The ISP can be found at a range of scales. In seismology, for instance, it can be applied to the recordings of major earthquakes<sup>1,2</sup> or microseismic events in the subsurface.<sup>3,4</sup> By retrieving the original wavefields throughout the subsurface, these sources can be localized and monitored, based on which the underlying source mechanisms can be revealed.<sup>5</sup> The ISP is also relevant in underwater acoustics<sup>6</sup> and ultrasonic non-destructive testing.<sup>7</sup> Although the methodology that is being discussed in this paper can be applied to any ISP, we pay special attention to Photo-Acoustic (PA) imaging, an emerging biomedical modality.<sup>8</sup> In PA imaging, a short pulse of light is emitted instantaneously into biological tissues, creating a distribution of simultaneously acting acoustic sources due to thermo-elastic conversion at those locations where the light is absorbed. The generated wavefield can be recorded outside the volume and the source distribution can be recovered by solving the ISP. PA imaging is based on the optical absorption properties of tissues, but can image orders of magnitude deeper than traditional optical imaging techniques.<sup>9</sup> These traditional techniques rely on ballistic photons, limiting the resolution to a single mean

free path of a photon (about 1 mm). In PA imaging, we send a nanosecond pulse of light into the tissue that rapidly becomes diffuse. The penetration depth of this diffuse beam of light can reach several centimeters. The resolution of PA imaging, however, is limited by the acoustic wavelength, which is dependent upon the size of the optical absorber and attenuation. The resulting PA image can be highly relevant for various applications, such as imaging vasculature for cancer detection<sup>10</sup> and monitoring.<sup>11</sup>

Traditionally, the ISP is solved by propagating the recorded signals backwards in time in a smooth model of the propagation velocity.<sup>12–14</sup> This principle can be understood intuitively by the analogy of a time-reversal mirror.<sup>15</sup> Since the acoustic wave equation is invariant for time-reversal (where we assume that attenuation is negligible), the recorded waveforms can be propagated backwards in time to reconstruct the source distribution. This result can be derived directly from Green's theorem.<sup>16,17</sup> From this theorem, we can also see that, in order to achieve accurate results in arbitrary heterogeneous media, wavefields should be backpropagated in the physical medium from a closed boundary. This could for instance be done by injecting the wavefields in the physical medium.<sup>15</sup> Alternatively, the fields can be backpropagated in a model. In most cases, the model is smooth and describes the propagation of the direct wavefield only, where scattering is typically ignored. Further, recordings are often acquired with a limited array only and, consequently, the closed boundary cannot be realized. These limitations can lead to artifacts and an incomplete solution of the ISP,

<sup>a)</sup>Electronic mail: [j.r.vanderneut@tudelft.nl](mailto:j.r.vanderneut@tudelft.nl)

especially in strongly heterogeneous media. Alternatively, the ISP can be posed as an optimization problem.<sup>18–20</sup> Although this approach can mitigate some of the problems that stem from incomplete recording devices, scattered arrivals are not accounted for by this procedure, unless the exact model is known.

Several attempts have been proposed to mitigate the artifacts that are caused by scattered arrivals during back-propagation and optimization. One of them is PAFUSion, which was introduced specifically for the practice of PA imaging and has been successfully demonstrated in a controlled lab experiment<sup>21</sup> and *in vivo*.<sup>22</sup> In this method, the acquired PA data are crosscorrelated with a multi-offset ultrasound reflection response, which is to be acquired at one side of the volume. By this procedure, scattering artifacts in a PA image can be predicted and eventually subtracted. Although encouraging results have been reported, the proposed approach assumes all PA direct source wavefields and their scattered contributions to be separated in time. Higher-order scattering and medium perturbations above the PA sources are not accounted for. We propose an alternative solution that is based on multiple crosscorrelations with the single-sided reflection response. Although we use similar input data as in PAFUSion, our result is correct for all orders of scattering and is valid even if multiple PA sources and their scattered components are interfering. To establish these results, we make use of a multidimensional Marchenko equation.<sup>23–26</sup> This equation has recently been obtained as an extension of its one-dimensional (1D) equivalent.<sup>27,28</sup> By solving the multidimensional Marchenko equation, we can retrieve the so-called focusing functions, which relate directly to the inverse transmission responses from the acquisition surface to the image points in the medium. By crosscorrelation of the retrieved focusing functions (rather than the PA data as is done in PAFUSion) with the reflection response, we find the solution of the ISP. In essence, an ideal focusing function is a wavefield that, when convolved with the recorded PA data, results in the original wavefield of the PA sources throughout the medium, free from artifacts caused by (single and multiple) scattering. Although this paper is mainly inspired by the practice of PA imaging, the results can be applied to any ISP, given that multi-channel reflection data are available. To acquire the multi-channel data, multiple sources and multiple receivers should be densely distributed over a finite acquisition aperture, obeying the Nyquist-Shannon sampling criterion.

This paper contains various sections. First, we define the ISP in Sec. II. To facilitate the derivations that follow, we introduce reciprocity theorems of the convolution and correlation type in Sec. III. In Sec. IV, we give a brief description of time-reversed acoustics, offering a conventional solution to the ISP.<sup>16,17</sup> To establish this solution, Green’s functions are required to propagate the observations from a closed boundary back into the medium. We illustrate the consequences of (1) using one-sided observations only and (2) the use of incomplete Green’s functions that lack the scattered components. In Sec. V, we evaluate PAFUSion,<sup>21,22</sup> which has been introduced recently to mitigate some of the problems that result from scattering. We demonstrate the PAFUSion methodology

with 1D synthetics and discuss its strength and limitations. In Sec. VI, we derive an alternative solution of the ISP, which is based on wavefield focusing from a single boundary of observations only. Unlike in time-reversed acoustics or PAFUSion, we assume additional knowledge of a so-called focusing function, being the solution of a multidimensional Marchenko equation. In Sec. VII, we derive this equation and we show how it can be solved, given that single-sided reflection data and a smooth model of the propagation velocity are given. We demonstrate the application of the methodology to solve ISPs in Sec. VIII and we present an alternative approach, based on adaptive subtraction, in Sec. IX. Finally, we provide a discussion on the strength and limitations of our solution in Sec. X.

## II. THE INVERSE SOURCE PROBLEM

In this paper, we assume that a distribution of sources is located inside a finite volume  $\mathcal{V}$ , as illustrated in Fig. 1. The volume is enclosed by a horizontal top surface  $\partial\mathcal{V}_1$ , a horizontal bottom surface  $\partial\mathcal{V}_2$  and a cylindrical surface  $\partial\mathcal{V}_{\text{cyl}}$ , where the radius of the cylinder approaches infinity, i.e.,  $r_{\text{cyl}} \rightarrow \infty$ . We assume that the medium is homogeneous outside  $\mathcal{V}$ , such that the boundaries  $\partial\mathcal{V}_1$  and  $\partial\mathcal{V}_2$  are transparent. Since the multidimensional Marchenko equation can also be derived for a configuration with a free surface at  $\partial\mathcal{V}_1$ ,<sup>29</sup> the theory that is derived in this paper can be extended for this specific configuration. We define a 3D Cartesian coordinate system for the spatial coordinates:  $\mathbf{x} = (x, y, z)$ . In our notation, we use bold characters to denote multidimensional quantities and regular characters for scalars. Since many of the operations that occur in this paper involve integrals over horizontal coordinates  $x$  and  $y$ , we define an additional symbol  $\boldsymbol{\chi} = (x, y)$  such that  $\mathbf{x} = (\boldsymbol{\chi}, z)$ . The source distribution is given by  $s(\mathbf{x}_S, t)$ , indicating the source strength as a function of source location  $\mathbf{x}_S = (x_S, y_S, z_S)$  and time  $t$ , where  $\mathbf{x}_S \in \mathcal{V}$ . It is assumed that all sources emit a signal of finite temporal bandwidth simultaneously at  $t=0$ . At this moment, we assume that the emitted signals are zero-phase, such that  $s(\mathbf{x}_S, t) = s(\mathbf{x}_S, -t)$ . The consequences of non-zero phase

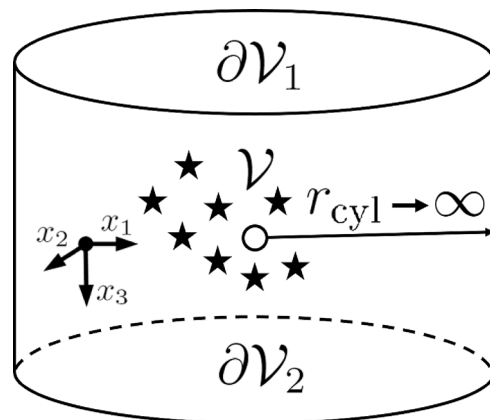


FIG. 1. Configuration: a cylindrical volume  $\mathcal{V}$  is bounded by an upper plane  $\partial\mathcal{V}_1$  (at depth  $z_1$ ), a lower plane  $\partial\mathcal{V}_2$  (at depth  $z_2$ ), and a cylindrical surface  $\partial\mathcal{V}_{\text{cyl}}$ , where the radius of the cylinder approaches infinity:  $r_{\text{cyl}} \rightarrow \infty$ . The black stars indicate source locations.

source signatures will be discussed in Sec. X. The sources generate a wavefield, propagating through the medium, which is defined in terms of its density  $\rho(\mathbf{x})$  and propagation velocity  $c(\mathbf{x})$ . It is assumed that the medium is lossless. To describe the generated wavefield, we make use of Green's functions  $G(\mathbf{x}|\mathbf{x}_S, t)$ , which are defined as the responses of impulsive sources at locations  $\mathbf{x}_S$ , according to the following wave equation<sup>30</sup>

$$\left\{ \left( \rho(\mathbf{x}) \nabla \cdot (\rho^{-1}(\mathbf{x}) \nabla) - \frac{1}{c^2(\mathbf{x})} \frac{\partial^2}{\partial t^2} \right) G \right\} (\mathbf{x}|\mathbf{x}_S, t) = -\rho(\mathbf{x}) \delta(\mathbf{x} - \mathbf{x}_S) \frac{\partial \delta(t)}{\partial t}, \quad (1)$$

where  $\nabla = (\partial/\partial x, \partial/\partial y, \partial/\partial z)$ . On the right-hand side, we find a 1D delta function in time  $\delta(t)$  and a 3D delta function in space  $\delta(\mathbf{x} - \mathbf{x}_S)$ , which should be interpreted as  $\delta(x - x_S)\delta(y - y_S)\delta(z - z_S)$ . We define the solution to be causal, such that  $G(\mathbf{x}|\mathbf{x}_S, t) = 0$  for  $t < 0$ . The wavefield that is produced by the source distribution can be described by the following volume integral equation:

$$p(\mathbf{x}, t) = \int_{\mathcal{V}} d^3\mathbf{x}_S G(\mathbf{x}|\mathbf{x}_S, t) * s(\mathbf{x}_S, t), \quad (2)$$

where  $*$  denotes temporal convolution. Our aim is to reconstruct the pressure field throughout the volume from observations outside the volume and to evaluate the result in the limit  $t \rightarrow 0$ . In practice, however, it appears easier to retrieve the quantity

$$I(\mathbf{x}, t) = \frac{1}{2}p(\mathbf{x}, t) + \frac{1}{2}p(\mathbf{x}, -t). \quad (3)$$

We refer to  $I(\mathbf{x}, t)$  as the reconstructed pressure field. By evaluating  $I(\mathbf{x}, t)$  at  $t=0$ , we can create an image of the source distribution. For a quantitative interpretation of this image, we describe the Green's function locally by the following spherical solution of the wave equation:<sup>30</sup>

$$G(\mathbf{x}|\mathbf{x}_S, t) \approx \frac{\rho(\mathbf{x}_S)}{4\pi|\mathbf{x} - \mathbf{x}_S|} \frac{\partial}{\partial t} \delta(t - |\mathbf{x} - \mathbf{x}_S|/c(\mathbf{x}_S)). \quad (4)$$

In this approximation, we have assumed that the medium is locally homogeneous in the vicinity of the source. By substitution of Eq. (4) into Eq. (2) and the result into Eq. (3), it can be derived that

$$I(\mathbf{x}, t)|_{t=0} \approx \int_{\mathcal{V}} d^3\mathbf{x}_S \frac{\rho(\mathbf{x}_S)}{4\pi|\mathbf{x} - \mathbf{x}_S|} \frac{\partial}{\partial t} s \left( \mathbf{x}_S, t - \frac{|\mathbf{x} - \mathbf{x}_S|}{c(\mathbf{x}_S)} \right) \Big|_{t=0}, \quad (5)$$

where we have assumed that  $s(\mathbf{x}_S, t) = s(\mathbf{x}_S, -t)$ . Note that the result can be interpreted as an image of the source distribution, which is blurred spatially because of (1) the spatial distribution of the sources and (2) their finite temporal bandwidth. Throughout the paper, we will refer to the image  $I(\mathbf{x}, t)|_{t=0}$  as the solution of the ISP. Our aim is to retrieve this solution at each location  $\mathbf{x}$  inside a discretized computational

domain  $\mathcal{D}$ . The computational domain can be identical to  $\mathcal{V}$  or it can be an arbitrary subset of  $\mathcal{V}$ . Since the solution of the ISP is proportional to the source distribution, it can be used for structural imaging. In PA imaging, for instance, the solution of the ISP leads to a structural image of the absorbed light in the tissue.

### III. RECIPROCITY THEOREMS

In the derivations that follow, we make use of reciprocity theorems. For notational convenience, we express these theorems in the frequency domain. For this purpose, we define the following temporal Fourier transform, where  $\omega$  denotes the angular frequency:

$$p(\mathbf{x}, \omega) = \int_{-\infty}^{\infty} dt p(\mathbf{x}, t) \exp(-j\omega t). \quad (6)$$

In the reciprocity theorems, wavefields in one state (A) are related to wavefields in another state (B). Throughout the paper, we make use of the configuration, which is shown in Fig. 1. The medium properties in states A and B are the same. The following reciprocity theorem of the convolution type<sup>30,31</sup> can be derived:

$$\int_{\mathcal{V}} d^3\mathbf{x} (p_A q_B - q_A p_B) = - \int_{\partial\mathcal{V}_1} d^2\boldsymbol{\chi} (p_A v_{zB} - v_{zA} p_B) + \int_{\partial\mathcal{V}_2} d^2\boldsymbol{\chi} (p_A v_{zB} - v_{zA} p_B). \quad (7)$$

Here,  $p_A$ ,  $v_{zA}$ , and  $q_A$  are the pressure, vertical particle velocity and source wavefields in state A. Similar quantities are defined in state B. On the left-hand side of the equation, 3D integration takes place over the volume  $\mathcal{V}$ . On the right-hand side, 2D integration takes place over the enclosing boundaries  $\partial\mathcal{V}_1$  and  $\partial\mathcal{V}_2$ . An additional integral over  $\partial\mathcal{V}_{\text{cyl}}$  is absent on the right-hand side, since its contribution vanishes for  $r_{\text{cyl}} \rightarrow \infty$ . This is because the integrand of this integral decays by an order of  $\mathcal{O}(r_{\text{cyl}}^{-2})$ , while its surface  $\partial\mathcal{V}_{\text{cyl}}$  grows by an order of only  $\mathcal{O}(r_{\text{cyl}})$ . A similar reciprocity theorem can be formulated of the correlation type,<sup>31,32</sup> where the integral over  $\partial\mathcal{V}_{\text{cyl}}$  vanishes for similar reasons:

$$\int_{\mathcal{V}} d^3\mathbf{x} (p_A^* q_B + q_A^* p_B) = - \int_{\partial\mathcal{V}_1} d^2\boldsymbol{\chi} (p_A^* v_{zB} + v_{zA}^* p_B) + \int_{\partial\mathcal{V}_2} d^2\boldsymbol{\chi} (p_A^* v_{zB} + v_{zA}^* p_B). \quad (8)$$

In this equation, superscript  $*$  stands for complex conjugation. Since complex conjugation in the frequency domain is equivalent to time reversal in the time domain, the products that are expressed in the frequency domain in Eq. (8) represent crosscorrelations in the time domain. On the other hand, the products that are expressed in the frequency domain in Eq. (7) represent convolutions in the time domain.

### IV. TIME REVERSED ACOUSTICS

Traditionally, the ISP has been solved by backpropagating wave recordings from a closed boundary. The theory for

this approach can be derived straightforwardly from the reciprocity theorem of the correlation type. We define an impulsive source  $Q_A = \delta(\mathbf{x} - \mathbf{x}_F)$  at location  $\mathbf{x}_F \in \mathcal{V}$  in state A. The pressure field is expressed by the Green's function  $p_A = G(\mathbf{x}|\mathbf{x}_F, \omega)$ . The particle velocity field is given by an alternative Green's function  $v_{zA} = G_z(\mathbf{x}|\mathbf{x}_F, \omega)$ , which is related to  $G$  by the equation of motion:<sup>30</sup>

$$G_z(\mathbf{x}|\mathbf{x}_F, \omega) = -\frac{1}{j\omega\rho(\mathbf{x})} \frac{\partial G(\boldsymbol{\chi}, z|\mathbf{x}_F, \omega)}{\partial z}. \quad (9)$$

In state B, we place an impulsive source  $Q_B = \delta(\mathbf{x} - \mathbf{x}_S)$  at location  $\mathbf{x}_S$ , leading to similar Green's functions  $p_B = G(\mathbf{x}|\mathbf{x}_S, \omega)$  and  $v_{zB} = G_z(\mathbf{x}|\mathbf{x}_S, \omega)$ . Substituting these quantities into Eq. (8), it follows that

$$\Re\{G(\mathbf{x}_F|\mathbf{x}_S, \omega)\} = -\int_{\partial\mathcal{V}_1} d^2\boldsymbol{\chi} G^*(\mathbf{x}_F|\boldsymbol{\chi}, z_1, \omega) G_z(\boldsymbol{\chi}, z_1|\mathbf{x}_S, \omega) + \int_{\partial\mathcal{V}_2} d^2\boldsymbol{\chi} G^*(\mathbf{x}_F|\boldsymbol{\chi}, z_2, \omega) G_z(\boldsymbol{\chi}, z_2|\mathbf{x}_S, \omega). \quad (10)$$

To arrive at this result, we have applied source-receiver reciprocity<sup>31</sup>  $G(\mathbf{x}|\mathbf{x}_F, \omega) = G(\mathbf{x}_F|\mathbf{x}, \omega)$ . Moreover, we have assumed that the medium is reflection-free above  $\partial\mathcal{V}_1$  and below  $\partial\mathcal{V}_2$ , such that the two terms in the integrands in the right-hand side of Eq. (8) gave identical contributions and could be summed, where the evanescent wavefield has been neglected.<sup>17</sup> Equation (10) has been used extensively in time-reversed acoustics to reconstruct the response in the interior of the volume by a set of observations outside the volume.<sup>13,14</sup> To illustrate this concept, we multiply Eq. (10) with the source distribution  $s(\mathbf{x}_S, \omega)$  and we integrate over  $\mathbf{x}_S$ . With help of the definitions in Eqs. (2), (3), and (9), it follows that

$$I(\mathbf{x}_F, \omega) = -\int_{\partial\mathcal{V}_1} d^2\boldsymbol{\chi} \overbrace{G^*(\mathbf{x}_F|\boldsymbol{\chi}, z_1, \omega)}^{\text{propagator}} \overbrace{v_z(\boldsymbol{\chi}, z_1, \omega)}^{\text{data}} + \int_{\partial\mathcal{V}_2} d^2\boldsymbol{\chi} \overbrace{G^*(\mathbf{x}_F|\boldsymbol{\chi}, z_2, \omega)}^{\text{propagator}} \overbrace{v_z(\boldsymbol{\chi}, z_2, \omega)}^{\text{data}}. \quad (11)$$

On the right-hand side,  $v_z(\boldsymbol{\chi}, z_1, \omega)$  and  $v_z(\boldsymbol{\chi}, z_2, \omega)$  are the particle velocity observations at levels  $z_1$  and  $z_2$ , respectively. These fields are related to the pressure fields by the equation of motion:  $v_z(\mathbf{x}, \omega) = -(1/j\omega\rho(\mathbf{x}))[\partial p(\boldsymbol{\chi}, z, \omega)/\partial z]$ . The Green's functions  $G^*(\mathbf{x}_F|\boldsymbol{\chi}, z_1, \omega)$  and  $G^*(\mathbf{x}_F|\boldsymbol{\chi}, z_2, \omega)$  in Eq. (11) propagate the observed data backward in time to an arbitrary location  $\mathbf{x}_F$  inside the volume. As we can learn from the left-hand side of the equation, this operation results in the reconstructed pressure field  $I(\mathbf{x}_F, \omega)$ , as we defined it in Eq. (3). After inverse Fourier transformation and evaluation of  $I(\mathbf{x}_F, t)|_{t=0}$ , we can obtain an image of the initial source distribution, as we discussed earlier.

Next, we illustrate how Eq. (11) can be used to propagate wavefield observations from the boundaries  $\partial\mathcal{V}_1$  and  $\partial\mathcal{V}_2$  back into the volume, given that the Green's functions of the medium are known. However, as we mentioned in the

Introduction, it is not uncommon that data are only available at the upper boundary  $\partial\mathcal{V}_1$  and that the Green's functions (which ought to be computed in the physical medium) are computed in a smooth model. Our aim is to investigate the consequences of these simplifications, using an example from PA imaging, which is equivalent to a lab experiment that has been conducted before to illustrate the concept of PAFUSion.<sup>21</sup> Although the theory that we derived is valid for 2D and 3D implementations, we restrict ourselves to 1D simulations throughout this paper. The propagation velocity in this example is fixed at  $c = 1500$  m/s, but a perturbation is introduced in the density model, as shown in Fig. 2(a). The computational domain  $\mathcal{D}$  is equal to the volume  $\mathcal{V}$  and contains 2001 spatial samples with 0.01 mm spacing. The volume is enclosed by transparent boundaries at  $z_1 = 0$  mm and  $z_2 = 20$  mm. A strong PA source is located above the perturbation at  $z_{S1} = 5$  mm and a weak PA source is located below the perturbation at  $z_{S2} = 12.3$  mm. The source strengths are chosen such that the initial pressure at the upper source location equals  $p(z_{S1}, t \rightarrow 0) = 1$  kPa, while for the weaker source  $p(z_{S2}, t \rightarrow 0) = 0.25$  kPa. The PA wavefields are computed and visualized in Fig. 2(b). The particle velocity field is recorded at  $z_1$ , resulting in the data trace that is shown in Fig. 2(c). Note that this trace is a scaled version of the pressure field via  $v_z(z, t) = (\rho(z)c(z))^{-1}p(z, t)$  in this 1D example. We have indicated the direct waves of the PA sources in the figure. The other arrivals indicate reflections. Our objective is to image  $I(z, t)|_{t=0}$ . Since the chosen source wavelet is symmetric in time, this result is equivalent to the excited

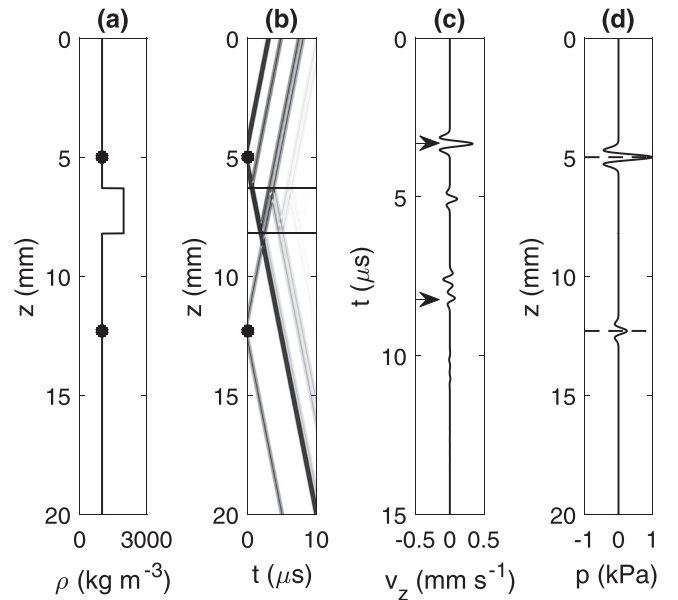


FIG. 2. (a) Density  $\rho(z)$  as a function of depth  $z$ . The black dots denote two PA sources, where the amplitude of the lower source is four times as weak as the amplitude of the upper source. (b) The acoustic pressure field  $p(z, t)$  as a function of depth  $z$  and time  $t$  for the PA experiment, where both PA sources are simultaneously ignited at  $t = 0$ . For visual purposes, the absolute value of the wavefield is shown. Solid black lines represent the borders of the density perturbation. (c) Recorded particle velocity field  $v_z(z = 0, t)$ . The direct waves of both PA sources are indicated by arrows. (d) Excited pressure field  $p(z, t)$  in the limit  $t \rightarrow 0$ . This is the solution of the ISP, as defined in this paper.

pressure field in the limit  $t \rightarrow 0$ . In Fig. 2(d), we show this desired image for reference.

Following the theory of time-reversed acoustics, we aim to solve the ISP by evaluating the right-hand side of Eq. (11), consisting of an integral over  $\partial\mathcal{V}_1$  and an integral over  $\partial\mathcal{V}_2$ . Note that these integrals reduce to scalar multiplications in a 1D medium. Since data are only recorded at the upper boundary, the contribution of  $\partial\mathcal{V}_2$  is typically neglected. Moreover, we tend to compute the required Green's functions for this operation in a smooth model, rather than in the physical medium. We define a model by a homogeneous fluid with velocity  $c = 1500$  m/s, without the presence of the density perturbation. We use the first term on the left-hand side of Eq. (11) to propagate the trace in Fig. 2(c) backwards in time. We apply inverse Fourier transformation and evaluate the result at  $t = 0$ , yielding the PA image that is shown in Fig. 3(a). We can clearly observe the locations of the PA sources, as indicated by the dashed black lines. However, we can also observe artifacts, as indicated by the arrows in the figure. Moreover, the PA amplitudes are not recovered correctly. In Fig. 3(b), we show the same result, when the Green's functions are computed in the physical medium (including the density perturbation), rather than in the homogeneous model. Compared to the result in Fig. 3(a), amplitudes are slightly different and additional artifacts have emerged, as indicated by the upper arrow in the figure. To remove all artifacts from this result, observations should also be included from the bottom of the medium. Hence, the contribution of  $\partial\mathcal{V}_2$  should also be computed, requiring additional data from  $z_2$ . We computed these data and evaluated the second term in the right-hand side of Eq. (11) [see Fig. 3(c)]. Note that the same

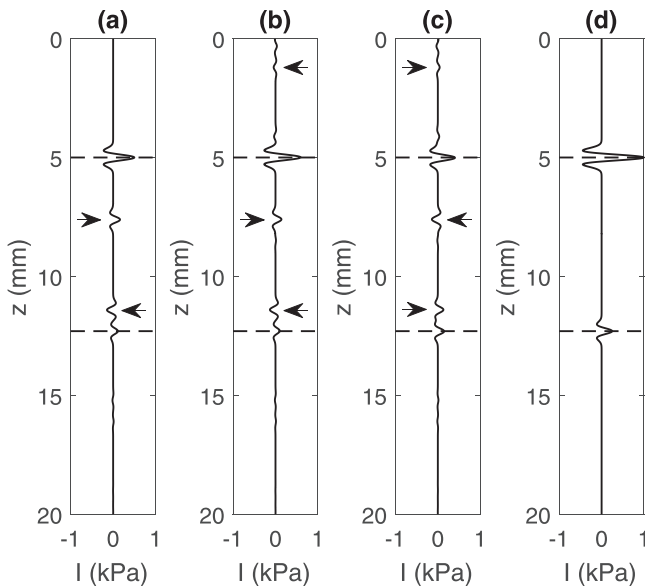


FIG. 3. (a) PA image [reconstructed pressure field  $I(z, t)|_{t=0}$ ] as derived from time-reversed acoustics with observations from the top of the medium only and Green's functions from a homogeneous model. (b) Same as (a), when using Green's functions from the physical medium. (c) Same as (b), when observations are used from the bottom of the medium only. (d) PA image that is obtained by summing (b) and (c), such that the required closed boundary is complete. The dashed lines indicate the PA source locations. The arrows point at artifacts.

artifacts emerge as in Fig. 3(b), but with reversed polarity. Hence, these artifacts are effectively eliminated when both traces are summed, as shown in Fig. 3(d). After this operation, both PA sources are clearly visible with their correct amplitudes. This result demonstrates that the ISP can indeed be solved by the implementation of Eq. (11), given that Green's functions are known in the physical medium and observations are used at both sides of the volume. In practice, observations are often available at a single boundary only and the exact model (including the perturbations) is generally not available. Consequently, Green's functions are typically computed in a smooth model, where single-sided observations are used, leading to the incomplete result that was shown in Fig. 3(a). From this result, it is impossible to distinguish for instance the weak lower PA source from the artifacts, which can easily lead to problems in interpretation. Moreover, this implementation does not restore the correct amplitudes of the PA sources, making quantitative photoacoustic imaging impossible in heterogeneous media.<sup>33</sup>

## V. PAFUSion

In PAFUSion, we aim to estimate scattering artifacts in a PA image by focusing an ultrasound beam at a PA source location. This can either be done by physical focusing<sup>21</sup> or by synthetic focusing,<sup>22</sup> using multi-offset ultrasound reflection data to be acquired at the acquisition surface. In this section, we discuss synthetic focusing only. To establish this methodology, the direct PA arrival of an individual PA source (or a distribution of sources) should be separated from all scattered contributions. All PA arrivals prior to a specified recording time  $t_g$  are isolated with a time gate and it is assumed that no scattered arrivals occur at  $t < t_g$ . As an example, we show the synthetic PA data that was discussed before in Fig. 4(a), with  $t_g = 4 \mu\text{s}$ , such that only the direct wavefield of the upper PA source is isolated by the time gate. Next, the isolated wavefield is crosscorrelated with the reflection response at the acquisition surface. By this operation, the traveltime from the acquisition surface to the upper PA source is subtracted from the two-way traveltimes of the reflections (as recorded at the acquisition surface). This yields a prediction of the reflections that are produced by the upper PA source. This prediction is shown in Fig. 4(b). As indicated by the arrows, we can indeed predict some of the undesired events in Fig. 4(a) by this procedure. This can be understood intuitively: by crosscorrelating the time-gated PA arrival with the reflection response, we have generated a virtual (downgoing) source at the PA location and recorded its upgoing scattered components. However, from this intuitive interpretation we can also learn that only artifacts from scattering below the PA source can be predicted and that interference of PA signals from multiple depth levels can pose limitations, as the selection of  $t_g$  will not always be trivial or at all possible.

In Fig. 4(c), we show the results after the predicted artifacts have been subtracted from the acquired PA data. Finally, we propagate these data back into the medium, using Green's functions from a homogeneous model with a propagation velocity of 1500 m/s. This yields the updated PA

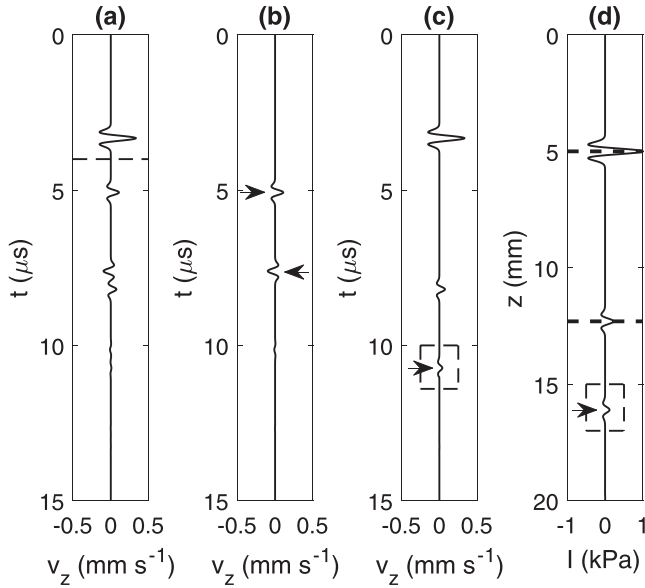


FIG. 4. (a) PA data [recorded particle velocity field  $v_z(z, t)|_{z=0}$ ]. The direct wavefield from the shallow PA source arrives earlier than  $t_g$ , which is indicated by the dashed black line. After isolation by the time gate, this wavefield is crosscorrelated with the reflection response to estimate (b) the PAFUSion prediction. The arrows point at the predicted artifacts. (c) The PA data, after the predicted artifacts have been subtracted. (d) The PA image [reconstructed pressure field  $I(z, t)|_{z=0}$ ] by backpropagation with Green's functions from a homogeneous model, using the PA data from (c). The arrows in (c) and (d) indicate an artifact from the lower PA source, which is not treated by the procedure. The black boxes in these figures have been amplified with a factor 5.

image in Fig. 4(d). Akin to the results in Fig. 3(a), observations have been used at  $\partial\mathcal{V}_1$  (corresponding to a single point in this 1D example) only. Note that several of the artifacts that appear in Fig. 3(a) are not observed in Fig. 4(d), demonstrating the success of PAFUSion. On the other hand, the arrows in Fig. 4(c) and Fig. 4(d) point at an artifact, which has not been tackled by the described procedure. This artifact is caused by the lower and weaker PA source, which is located below the density perturbation. As we will show in Sec. X, this type of artifact can be much more pronounced in different scenarios, for instance when strong PA sources are located below the significant perturbations in the medium. In Secs. VI and VII, we derive a procedure that does not require to set a time-gate  $t_g$ . Unlike PAFUSion, our solution is valid for all orders of scattering and solves for the artifacts from a spatial distribution of simultaneously acting PA sources, which can be arbitrarily distributed in the volume.

## VI. THEORY OF SINGLE-SIDED WAVEFIELD FOCUSING

In this section, we derive a solution of the ISP, based on single-sided wavefield focusing. To facilitate our derivation, we decompose wavefields in terms of their upgoing (indicated by superscript  $-$ ) and downgoing (indicated by superscript  $+$ ) constituents. These constituents are normalized such that  $p = p^+ + p^-$  and  $v_z = v_z^+ + v_z^-$ . First, we decompose the wavefields in the right-hand side of the reciprocity theorem of the convolution type [Eq. (7)]. We can write the result as

$$\int_{\mathcal{V}} d^3\mathbf{x} (p_A q_B - q_A p_B) = -2 \int_{\partial\mathcal{V}_1} d^2\boldsymbol{\chi} (p_A^+ v_{zB}^- + p_A^- v_{zB}^+) - 2 \int_{\partial\mathcal{V}_2} d^2\boldsymbol{\chi} (v_{zA}^+ p_B^- + v_{zA}^- p_B^+). \quad (12)$$

Here, we have used the fact that convolutions of wavefield constituents that propagate in the same direction cancel each other when the decomposed integral is evaluated, while convolutions of wavefield constituents that propagate in opposite directions can be summed.<sup>31</sup> A similar decomposition can be applied to the right-hand side of the reciprocity theorem of the correlation type [Eq. (8)]. This time, all crosscorrelations of wavefield constituents that propagate in opposite directions cancel each other, while all crosscorrelations of wavefield constituents that propagate in the same direction can be summed.<sup>31</sup> The result can be written as

$$\int_{\mathcal{V}} d^3\mathbf{x} (p_A^* q_B + q_A^* p_B) = -2 \int_{\partial\mathcal{V}_1} d^2\boldsymbol{\chi} (p_A^{*+} v_{zB}^+ + p_A^{-*} v_{zB}^-) + 2 \int_{\partial\mathcal{V}_2} d^2\boldsymbol{\chi} (v_{zA}^{*+} p_B^+ + v_{zA}^{-*} p_B^-). \quad (13)$$

To establish single-sided wavefield focusing, we introduce the so-called focusing function  $f_1(\mathbf{x}|\mathbf{x}_F, t)$ , which is emitted into the medium from the upper boundary. This focusing function is defined as a wavefield that focuses at the focal point  $\mathbf{x}_F = (\boldsymbol{\chi}_F, z_F)$ . Although the focal point is given as an argument of the focusing function, the function does not have a source at this (or any other) location. It is a solution of the source-free wave equation [i.e. Eq. (1) with the right-hand side equal to zero]. This wave equation is defined in a reference medium, which is identical to the physical medium, but reflection-free below  $z_F$ . Its solution is subject to a so-called focusing condition. To define this condition, we decompose  $f_1$  into its down- and upgoing constituents, where  $f_1 = f_1^+ + f_1^-$ , and we transform these quantities to the frequency domain. The focusing condition dictates that the downgoing particle velocity field at the focal point is given by<sup>23</sup>

$$v_{zA}^+(\boldsymbol{\chi}, z, \omega)|_{z=z_F} = -\frac{1}{j\omega\rho} \frac{\partial f_1^+(\boldsymbol{\chi}, z|\mathbf{x}_F, \omega)}{\partial z} \Big|_{z=z_F} = \frac{1}{2} \delta(\boldsymbol{\chi} - \boldsymbol{\chi}_F). \quad (14)$$

In this definition,  $\delta(\boldsymbol{\chi} - \boldsymbol{\chi}_F)$  is a 2D Dirac delta function. Since the reference medium where the focusing function is defined is reflection-free below  $z_F$ , the upgoing particle velocity field vanishes at the focal point, according to  $v_{zA}^-(\boldsymbol{\chi}, z, \omega)|_{z=z_F} = 0$ . The focusing function can be used to project the recorded data from a single-sided boundary to the focal point. To demonstrate this concept, we make use of the partially decomposed reciprocity theorems in Eqs. (12) and (13), where we set  $z_2 = z_F$ . The physical and reference media are assumed to be reflection-free above  $z_1$ . In state A, we substitute the focusing function, leading to the pressure field  $p_A^\pm = f_1^\pm(\mathbf{x}|\mathbf{x}_F, \omega)$  and an associated particle velocity field.

Since the focusing function is a solution of the source-free wave equation, it follows that  $q_A = 0$  throughout the volume. In state B, we place an impulsive source at  $\mathbf{x}_S = (\boldsymbol{\chi}_S, z_S)$  (where  $z_S > z_1$ ), i.e.,  $q_B = \delta(\mathbf{x} - \mathbf{x}_S)$ . By substituting the relevant quantities into Eqs. (12) and (13), we can derive that

$$G^-(\mathbf{x}_F|\mathbf{x}_S, \omega) + H(z_F - z_S)f_1(\mathbf{x}_S|\mathbf{x}_F, \omega) = -2 \int_{\partial\mathcal{V}_1} d^2\boldsymbol{\chi} f_1^+(\boldsymbol{\chi}, z_1|\mathbf{x}_F, \omega) G_z(\boldsymbol{\chi}, z_1|\mathbf{x}_S, \omega), \quad (15)$$

and

$$G^+(\mathbf{x}_F|\mathbf{x}_S, \omega) - H(z_F - z_S)f_1^*(\mathbf{x}_S|\mathbf{x}_F, \omega) = 2 \int_{\partial\mathcal{V}_1} d^2\boldsymbol{\chi} f_1^{-*}(\boldsymbol{\chi}, z_1|\mathbf{x}_F, \omega) G_z(\boldsymbol{\chi}, z_1|\mathbf{x}_S, \omega). \quad (16)$$

Note that the lower boundary  $\partial\mathcal{V}_2$  of volume  $\mathcal{V}$  depends on the depth of the focal point  $z_2 = z_F$ . Hence,  $\mathbf{x}_S$  is only located inside the integration volume if  $z_S < z_F$ . As a consequence, the second term on the left-hand side vanishes if  $z_S \geq z_F$ . This is described by the Heaviside function  $H(z_F - z_S)$  in Eqs. (15) and (16), where  $H(z_F - z_S) = 1$  if  $z_S < z_F$ ,  $H(z_F - z_S) = 1/2$  if  $z_S = z_F$  and  $H(z_F - z_S) = 0$  if  $z_S > z_F$ . From Eqs. (15) and (16), it can be learned that the up- and downgoing Green's functions at location  $\mathbf{x}_F$  due to a source at  $\mathbf{x}_S$  can be retrieved by convolving the observations at the upper surface  $\partial\mathcal{V}_1$  with the downgoing focusing function and the time-reversed upgoing focusing function, respectively. To obtain the full Green's function, Eqs. (15) and (16) can be summed, yielding

$$G(\mathbf{x}_F|\mathbf{x}_S, \omega) + 2j\Im\{f_2(\mathbf{x}_F|\mathbf{x}_S, \omega)\}H(z_F - z_S) = -2 \int_{\partial\mathcal{V}_1} d^2\boldsymbol{\chi} f_2(\mathbf{x}_F|\boldsymbol{\chi}, z_1, \omega) G_z(\boldsymbol{\chi}, z_1|\mathbf{x}_S, \omega), \quad (17)$$

where we have defined a second type of focusing function<sup>23</sup> as

$$f_2(\mathbf{x}_F|\mathbf{x}, \omega) = f_1^+(\mathbf{x}|\mathbf{x}_F, \omega) - f_1^{-*}(\mathbf{x}|\mathbf{x}_F, \omega). \quad (18)$$

Now, we consider once again a distribution of sources  $s(\mathbf{x}_S, \omega)$ , where  $\mathbf{x}_S \in \mathcal{V}$ . By convolving Eq. (17) with this distribution and integrating  $\mathbf{x}_S$  over the volume  $\mathcal{V}$ , we obtain

$$p(\mathbf{x}_F, \omega) + 2j \int_{\mathcal{V}} d^3\mathbf{x}_S \Im\{f_2(\mathbf{x}_F|\mathbf{x}_S, \omega)\} s(\mathbf{x}_S, \omega) H(z_F - z_S) = -2 \int_{\partial\mathcal{V}_1} d^2\boldsymbol{\chi} \overbrace{f_2(\mathbf{x}_F|\boldsymbol{\chi}, z_1, \omega)}^{\text{propagator}} \overbrace{v_z(\boldsymbol{\chi}, z_1, \omega)}^{\text{data}}. \quad (19)$$

As we can learn from Eq. (19), observations  $v_z$  at a single side of the volume can be convolved with the focusing function  $f_2$  in order to retrieve the forward-propagating wavefield  $p(\mathbf{x}_F, \omega)$  in the interior of the volume. However, we also find an additional volume integral on the left-hand side if  $z_S \leq z_F$ . Since we assumed that the sources emit instantaneous signals at  $t = 0$ , the source distribution  $s(\mathbf{x}_S, \omega)$  is purely real-valued and consequently, the volume integral in Eq. (19) is

purely imaginary. Therefore, taking the real part of the equation yields with help of the definition in Eq. (3):

$$I(\mathbf{x}_F, \omega) = -\Re \left\{ \int_{\partial\mathcal{V}_1} \overbrace{d^2\boldsymbol{\chi} f_2(\mathbf{x}_F|\boldsymbol{\chi}, z_1, \omega)}^{\text{propagator}} \overbrace{v_z(\boldsymbol{\chi}, z_1, \omega)}^{\text{data}} \right\}. \quad (20)$$

A similar representation can be derived for quantummechanical, electromagnetic and elastodynamic waves by using a unified single-sided homogeneous Green's function representation.<sup>34</sup> The source distribution (i.e. the solution of the ISP) can be obtained by transforming  $I(\mathbf{x}_F, \omega)$  to the time domain and evaluating the result at  $t = 0$ . Now, we show how Eq. (20) can be used to solve the ISP from single-sided observations, given that the focusing function  $f_2$  is known. In Fig. 5(a), we show the focusing function as a function of depth of the focal point  $z = z_F$  and time  $t$ , for the medium that is shown in Fig. 2(a). This focusing function has been computed directly, using the transmission and reflection responses of reference media,<sup>26</sup> which have been truncated at  $z_F$ . In Sec. VII, we show how  $f_2$  can also be obtained from the multidimensional Marchenko equation, given that single-sided reflection data and a smooth model of the propagation velocity are known. In Fig. 5(b), we show the right-hand side of Eq. (19), after inverse Fourier transformation, as a function of  $t$  and  $z_F$ . As we can learn from the left-hand side of Eq. (19), this result can be interpreted as a superposition of the desired causal wavefield  $p(\mathbf{x}_F, t)$  and the contribution of an undesired volume integral. To remove the undesired contribution, we can take the real part of the wavefield, as in the right-hand side of Eq. (20). This operation leads to Fig. 5(c). The PA image can now be constructed by evaluation of this result at  $t = 0$ , see Fig. 5(d). Note that this result is highly

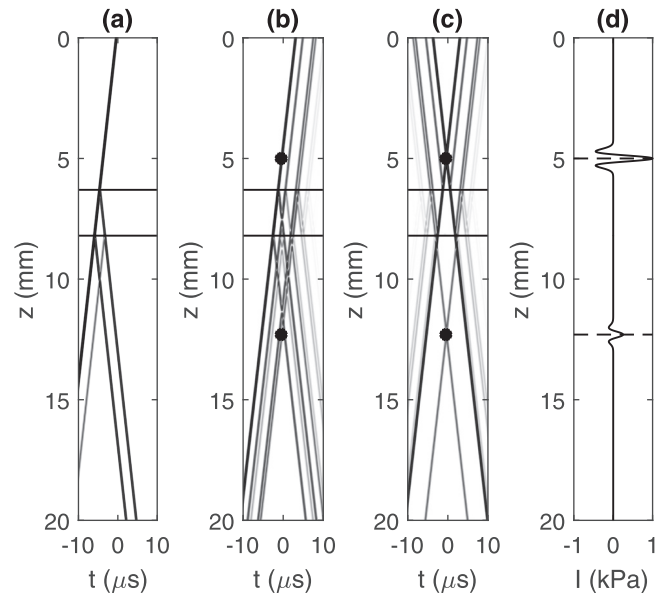


FIG. 5. (a) Focusing function  $f_2(z|0, t)$  as a function of depth  $z$  and time  $t$ . (b) Right-hand side of Eq. (19). (c) Right-hand side of Eq. (20). Solid black lines represent the borders of the density perturbation. (d) PA image [reconstructed pressure field  $I(z, t)|_{t=0}$ ] from single-sided focusing. The dashed lines indicate the true PA locations.

similar to the reference solution in Fig. 2(d). Unlike the solution in Fig. 3(d), i.e. the PA image from time-reversed acoustics, this result has been obtained from single-sided observations only. To achieve this, it has been assumed that  $f_2$  is known. In Sec. VII, we show how this focusing function can be obtained from single-sided reflection data and a smooth model of the propagation velocity.

## VII. THE MARCHENKO EQUATION

In this section, we show how focusing function  $f_2$  can be retrieved from single-sided reflection data and an estimate of the propagation velocity by solving the multidimensional Marchenko equation. The reflection data are indicated as  $R(\mathbf{x}|\mathbf{x}', t)$ , where  $\mathbf{x} = (\boldsymbol{\chi}, z)$  and  $\mathbf{x}' = (\boldsymbol{\chi}', z')$  indicate the receiver and source location, respectively. The reflection response is defined as the pressure response of a dipole source, according to<sup>23</sup>

$$R(\mathbf{x}|\mathbf{x}', t) = \frac{2}{j\omega\rho(\mathbf{x}')} \frac{\partial G^-(\mathbf{x}|\boldsymbol{\chi}', z', t)}{\partial z'}. \quad (21)$$

The receivers are distributed over the upper boundary  $\partial\mathcal{V}_1$  and the sources are positioned on the same boundary in the limit from the outside of  $\mathcal{V}$ . Consequently, the direct wavefield between a source and receiver is not included in the response. In practice, the reflection response is recorded in a finite frequency band and is encoded by a source signature. It is assumed that this source signature is known, such that the recorded data can be deconvolved, allowing us to retrieve  $R$  within a continuous, but finite, frequency band. In the following derivation, we apply various multidimensional convolutions of particular wavefields with the reflection response. To avoid notational clutter, we make use of the following notation to denote such an operation in the time domain:

$$\{\mathcal{R}p\}(\mathbf{x}, t) = \int_{\partial\mathcal{V}_1} d^2\boldsymbol{\chi}' R(\mathbf{x}|\boldsymbol{\chi}', z_1, t) * p(\boldsymbol{\chi}', z_1, t), \quad (22)$$

where  $\mathbf{x} \in \partial\mathcal{V}_1$ . In this expression,  $p(\mathbf{x}, t)$  is an arbitrary input wavefield at the acquisition level  $\partial\mathcal{V}_1$  and  $\mathcal{R}$  is an operator for multidimensional convolution with the reflection response. Another useful operator  $\mathcal{Z}$  is introduced to apply time-reversal, according to the definition

$$\{\mathcal{Z}p\}(\mathbf{x}, t) = p(\mathbf{x}, -t). \quad (23)$$

With help of these operators, the following representation can be derived<sup>23</sup>

$$\widehat{G}(\mathbf{x}_F|\mathbf{x}_S, t) = \{(\mathcal{Z} + \mathcal{R})\widehat{f}_2\}(\mathbf{x}_F|\mathbf{x}_S, t). \quad (24)$$

In this equation,  $G(\mathbf{x}_F|\mathbf{x}_S, t)$  is a Green's function, recorded at an arbitrary location  $\mathbf{x}_F = (\boldsymbol{\chi}_F, z_F)$  with  $z_F \geq z_1$ , where the source is positioned at the upper boundary  $\partial\mathcal{V}_1$ . Further,  $\widehat{f}_2(\mathbf{x}_F|\mathbf{x}_S, t)$  can be recognized as the focusing function that was discussed in Sec. VI. Both the Green's functions and focusing functions have been convolved with a wavelet  $W(t)$ , which is indicated by the  $\widehat{\cdot}$ -sign above the symbols.

This wavelet can be arbitrarily chosen, but its spectrum should be within the available bandwidth of the reflection response and it should be zero phase. It is assumed that the wavelet has a finite duration in the time domain, such that it is only non-zero in the interval  $[-t_w, t_w]$ . As we will discuss later,  $t_w$  poses an important limitation to the resolution of the proposed methodology. In all synthetic examples of this paper, we have chosen a Ricker wavelet with a center frequency of  $f_c = 2$  MHz and  $t_w = 1/f_c = 0.5 \mu\text{s}$ .

To retrieve the focusing function, we assume that it can be partitioned as  $f_2 = f_{2d} + f_{2m}$ . In this notation,  $f_{2d}$  is the direct part of the focusing function, describing direct propagation from the acquisition level  $\partial\mathcal{V}_1$  to the focal point, and  $f_{2m}$  is a coda, relating to (single and multiple) scattering in the medium. The direct part of the focusing function is closely related to the first event in the inverse of the transmission response.<sup>23</sup> In practice, we can approximate  $f_{2d}$  by a time-reversed Green's function, which is computed in a smooth model of the propagation velocity.<sup>25</sup> Offset-dependent transmission effects are not accounted for by this approximation, which can lead to amplitude errors and incomplete focusing in complex media.<sup>26</sup>

The key assumption from which the Marchenko equation can be derived is that the direct part of the focusing function is separated in time from its coda. This assumption is not always fulfilled in arbitrary heterogeneous media. It is strictly valid in media with smoothly curved interfaces,<sup>23</sup> which are sufficiently thin with respect to the available temporal bandwidth.<sup>24</sup> In media with sharp lateral contrasts and point diffractors, the direct part and the coda can overlap in time, which may result in artifacts when the Marchenko equation is evaluated in practice.<sup>26</sup> On the basis of the assumption of separation, we can design a window operator  $\Theta$  that mutes the constituents of any wavefield at  $t > t_d(\mathbf{x}_F|\mathbf{x}_S) - t_w$ , where  $t_d(\mathbf{x}_F|\mathbf{x}_S)$  is the traveltime of the direct wavefield at location  $\mathbf{x}_F$  in the medium due to a source at  $\mathbf{x}_S$ , while  $t_w$  is half the duration of the wavelet that was discussed before. The operator is symmetric in time, such that the constituents at  $t < -t_d(\mathbf{x}_F|\mathbf{x}_S) + t_w$  are also muted. Since all events in the Green's function arrive at or after the traveltime of the direct wave, it follows that  $\{\Theta\widehat{G}\}(\mathbf{x}_F|\mathbf{x}_S, t) = 0$ , as we illustrate in Fig. 6(a). For the focusing function, however, it can be shown that  $\{\Theta\widehat{f}_2\}(\mathbf{x}_F|\mathbf{x}_S, t) = \widehat{f}_{2m}(\mathbf{x}_F|\mathbf{x}_S, t)$ ,<sup>24,26</sup> see Fig. 6(b) (where it is assumed that the coda starts only after  $-t_d + t_w$  and hence is separated in time from the direct part of the focusing function). Consequently, the following result can be derived, after operators  $\Theta$  and  $\mathcal{Z}$  have been applied to Eq. (24):

$$-\{\mathcal{Z}\Theta\widehat{f}_{2d}\}(\mathbf{x}_F|\mathbf{x}_S, t) = \{(1 + \mathcal{Z}\Theta\mathcal{R})\widehat{f}_{2m}\}(\mathbf{x}_F|\mathbf{x}_S, t), \quad (25)$$

where we used the fact that  $\mathcal{Z}\Theta\mathcal{Z} = \Theta$ . Equation (25) is known as the multidimensional Marchenko equation.<sup>23,26</sup> Assuming that  $\widehat{f}_{2d}$  and the relevant operators can be estimated, we are left with only one unknown: the coda of the focusing function  $\widehat{f}_{2m}$ . To solve Eq. (25), we can

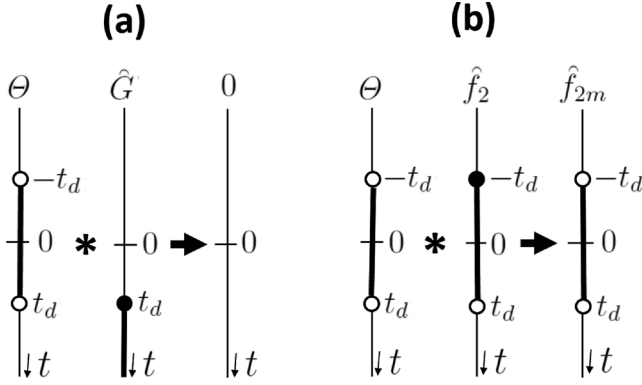


FIG. 6. (a) The muting operator  $\Theta$  passes only those entries with  $-t_d + t_w < t < t_d - t_w$  (where  $t_w$  ensures that the direct wave at  $+t_d$  or  $-t_d$  is also removed). The Green's function  $\hat{G}(t)$  is only non-zero for  $t \geq t_d$ . As illustrated, the wavefield vanishes when  $\Theta$  is applied to  $\hat{G}(t)$ . (b) The focusing function  $f_2(t)$  contains a direct part  $f_{2d}(t)$  at  $-t_d$  and a coda  $f_{2m}(t)$ , which is only non-zero for  $-t_d < t < t_d$ . As illustrated, the direct part vanishes when  $\Theta$  is applied to  $f_2(t)$ , while the coda remains.

apply iterative substitution, leading to the following Neumann series:

$$\hat{f}_{2m}(\mathbf{x}_F|\mathbf{x}_S, t) = \sum_{k=1}^{\infty} \hat{m}_k(\mathbf{x}_F|\mathbf{x}_S, t). \quad (26)$$

In this solution, the individual terms are defined as

$$\hat{m}_k(\mathbf{x}_F|\mathbf{x}_S, t) = \{(-\mathcal{Z}\Theta\mathcal{R})^k \hat{f}_{2d}\}(\mathbf{x}_F|\mathbf{x}_S, t). \quad (27)$$

With this result, we can retrieve the coda of the focusing function  $\hat{f}_{2m}$  from its direct part  $\hat{f}_{2d}$ , given that the operators  $\Theta$ ,  $\mathcal{R}$ , and  $\mathcal{Z}$  can be computed. Now, we illustrate this concept with the synthetic example that was discussed earlier in Fig. 2(a). We approximate the direct parts of the focusing functions by time-reversed Green's functions, which are computed in a homogeneous model with  $c = 1500$  m/s without density perturbations, see Fig. 7(a). Note that the same homogeneous model has been used to compute Fig. 3(a). In Fig. 7(b) and 6(c), we show the first and the second update of the coda of the focusing function, which have been computed with Eq. (27) for  $k=1$  and  $k=2$ , respectively. We computed ten updates of the focusing functions and summed them. On the basis of Eq. (26), this result can be interpreted as an estimate of  $\hat{f}_{2m}$ . In Fig. 7(d), we show this estimate, where the direct part of the focusing function has been added for completeness. Note that the result is highly similar to the true focusing function in Fig. 5(a). Because of the finite bandwidth of the data, truncations have been applied with  $t_w = 0.5 \mu\text{s}$ . As a consequence, the focusing function is not updated in the first  $z_w = c * t_w = 0.75$  mm below each reflector. This limitation is clearly visible just below the reflectors in Figs. 6(b) and 6(c), as indicated by the arrows in these figures. As a result, reverberations from thin layers cannot be resolved.<sup>24</sup> Despite this limitation with respect to high wave numbers, the methodology still works remarkably well for resolving the low wave number content of structures with many thin layers.<sup>35</sup> Because the transmission effects are not

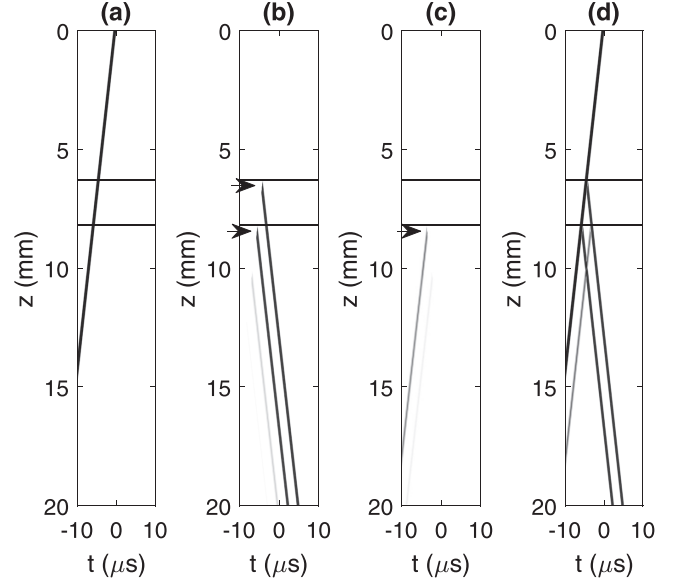


FIG. 7. (a) Direct part of the focusing function  $\hat{f}_{2d}$  as a function of depth  $z$  and time  $t$ , obtained in the smooth model. (b) First update of the coda  $\hat{m}_1$ . (c) Second update of the coda  $\hat{m}_2$ . Arrows indicate limitations that are posed by the finite bandwidth. (d) Estimate of the focusing function after the direct part and ten updates of the coda have been summed. Solid black lines represent the borders of the density perturbation.

accounted for in our estimate of the direct part of the focusing function, the amplitudes at each depth level are off by a scaling factor. This can be compensated for by an additional transmission effect correction.<sup>36</sup>

## VIII. APPLICATION OF SINGLE-SIDED WAVEFIELD FOCUSING

In this section, we demonstrate how the ISP can be solved by single-sided wavefield focusing. We start by transforming the individual terms in the series in Eq. (26) to the frequency domain and adding them to the direct part of the focusing function. The result can be substituted into Eq. (20), from which the following representation follows:

$$\begin{aligned} \hat{I}(\mathbf{x}_F, \omega) = & -\Re \left\{ \int_{\partial V_1} d^2 \chi \overbrace{\hat{f}_{2d}(\mathbf{x}_F|\chi, z_1, \omega)}^{\text{propagator}} \overbrace{v_z(\chi, z_1, \omega)}^{\text{data}} \right\} \\ & - \sum_{k=1}^{\infty} \Re \left\{ \int_{\partial V_1} d^2 \chi \overbrace{\hat{m}_k(\mathbf{x}_F|\chi, z_1, \omega)}^{\text{coda}} \overbrace{v_z(\chi, z_1, \omega)}^{\text{data}} \right\}. \end{aligned} \quad (28)$$

By evaluating the right-hand side of this equation,  $\hat{I}(\mathbf{x}_F, \omega)$  can be estimated. When this estimate is transformed to the time domain, the causal component can be interpreted as the retrieved wavefield  $\frac{1}{2}\hat{p}(\mathbf{x}_F, t)$ , see Fig. 8(a). Note that this result is highly similar to the original wavefield that was shown in Fig. 2(b), apart from the first  $z_w = c * t_w = 0.75$  mm below each reflector, where the focusing function has not been updated completely. This is a consequence of the window operator  $\Theta$  which has truncated wavefields at  $t = -t_d + t_w$ , rather than at  $t_d$  (the traveltime of the direct

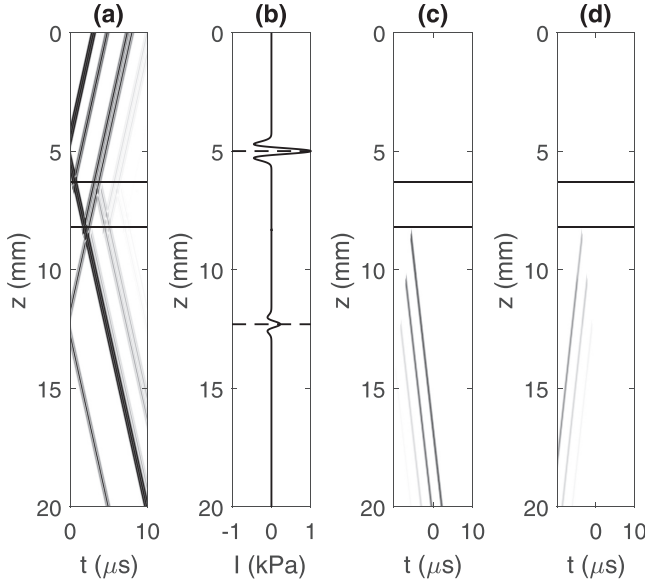


FIG. 8. (a) Reconstructed pressure wavefield  $\hat{I}(z, t)$  as retrieved by Eq. (28). Solid black lines represent the borders of the density perturbation. (b) PA image  $\hat{I}(z, t)|_{t=0}$  obtained by single-sided wavefield focusing. (c) Third update of the coda  $\hat{m}_3$ , amplified by a factor 5. (d) Fourth update of the coda  $\hat{m}_4$ , amplified by a factor 5.

wavefield). We can find the PA image by extracting the snapshot at  $t = 0$  from the reconstructed data  $\hat{I}(\mathbf{x}_F, t)$  [which is found by inverse Fourier transformation of Eq. (28)], see Fig. 8(b). Note that the locations of the PA sources can well be identified, without the obstruction of any artifacts. The amplitude of the lowest PA source has been slightly underestimated, which is caused by the incorrect amplitude of the direct part of the focusing function, where transmission effects have not been accounted for. As mentioned before, this can be improved by including an additional transmission effect correction.<sup>36</sup>

## IX. ADAPTIVE SUBTRACTION

Although the proposed methodology is powerful in theory, results are highly sensitive for the amplitude and phase of the reflection response, which is used to construct operator  $\mathcal{R}$ . Since each subsequent term in the evaluated series in Eq. (28) requires another round of multidimensional convolutions with  $\mathcal{R}$ , the signal quality tends to deteriorate fast when we evaluate higher-order updates.<sup>37,38</sup> Because of many unknowns, such as the source signature, transducer coupling, attenuation, elastic wave conversion, reflections from outside the volume, surface waves, etc. it appears to be difficult to fulfill the strong requirements to compute an accurate  $\mathcal{R}$ -operator. Moreover, in order to evaluate the integrals over  $\partial\mathcal{V}_1$  each time this operator is applied [see Eq. (22)], sufficient sources and receivers should be placed at this surface. Here, it is important that both the spacing should be sufficiently dense to avoid spatial aliasing and that all relevant offsets (being defined as the distances between sources and receivers) should be recorded in order to sample the stationary points of the integrals.<sup>26</sup> In seismic acquisition, for instance, the near offsets are typically not recorded and should be interpolated with high accuracy, making it difficult to construct  $\mathcal{R}$  in practice.<sup>38</sup> Finally, the computational

costs increase linearly with the number of terms that are evaluated in Eq. (28), making it desirable to keep this number as low as possible. This is especially relevant for applications in real time on large computational volumes.

By studying the higher-order updates of the coda  $\hat{m}_k$ , we find similar events as in the lower-order updates  $\hat{m}_1$  and  $\hat{m}_2$ . This is demonstrated for  $\hat{m}_3$  and  $\hat{m}_4$  in Figs. 8(c) and 8(d) [which contain the same events as Figs. 7(b) and 7(c) with significantly smaller amplitudes]. By interpreting the nature of the updates in more detail,<sup>24,26</sup> it can be learned that during the odd updates, the amplitudes of the downgoing components of the coda  $\hat{f}_2^+$  are updated, while during the even updates, the upgoing components of the coda  $\hat{f}_2^-$  are taken care of.<sup>24,26</sup> We may decide to truncate the series after the first two updates ( $\hat{m}_1$  and  $\hat{m}_2$ ) and then sum the individual terms, after applying adaptive filters  $a_1(\mathbf{x}_F, t)$  and  $a_2(\mathbf{x}_F, t)$  to them. These adaptive filters are assumed to accommodate for the fact that the series has been truncated. Further, these filters may compensate, to some extent, for inaccuracies of  $\mathcal{R}$ , in case this operator is estimated from band-limited data in the presence of noise. To facilitate this idea, the following representation can be derived from the inverse Fourier transform of Eq. (28):

$$\begin{aligned} \hat{I}(\mathbf{x}_F, t) \approx & \hat{I}_0(\mathbf{x}_F, t) + a_1(\mathbf{x}_F, t) * \hat{I}_1(\mathbf{x}_F, t) \\ & + a_2(\mathbf{x}_F, t) * \hat{I}_2(\mathbf{x}_F, t). \end{aligned} \quad (29)$$

In this result, the first term  $\hat{I}_0$  describes backpropagation of the acquired data from a single boundary with the initial focusing function:

$$\begin{aligned} \hat{I}_0(\mathbf{x}_F, t) = & - \int_{-\infty}^{+\infty} d\tau \int_{\partial\mathcal{V}_1} d^2\boldsymbol{\chi} \overbrace{\hat{\mathcal{F}}_{2d}(\mathbf{x}_F|\boldsymbol{\chi}, z_1, \tau)}^{\text{propagator}} \\ & \times \underbrace{(v_z(\boldsymbol{\chi}, z_1, t - \tau) + v_z(\boldsymbol{\chi}, z_1, -t - \tau))}_{\text{data}}. \end{aligned} \quad (30)$$

The other terms,  $\hat{I}_1$  and  $\hat{I}_2$  are meant to eliminate artifacts from multiple scattering. These terms can be found by substituting Eq. (27) into the inverse Fourier transform of Eq. (28), leading to

$$\begin{aligned} \hat{I}_1(\mathbf{x}_F, t) = & \int_{-\infty}^{+\infty} d\tau \int_{\partial\mathcal{V}_1} d^2\boldsymbol{\chi} \overbrace{\{\mathcal{ZOR}\hat{\mathcal{F}}_{2d}\}(\mathbf{x}_F|\boldsymbol{\chi}, z_1, \tau)}^{\text{coda}} \\ & \times \underbrace{(v_z(\boldsymbol{\chi}, z_1, t - \tau) + v_z(\boldsymbol{\chi}, z_1, -t - \tau))}_{\text{data}}, \end{aligned} \quad (31)$$

and

$$\begin{aligned} \hat{I}_2(\mathbf{x}_F, t) = & - \int_{-\infty}^{+\infty} d\tau \int_{\partial\mathcal{V}_1} d^2\boldsymbol{\chi} \\ & \times \overbrace{\{\mathcal{ZOR}\mathcal{ZOR}\hat{\mathcal{F}}_{2d}\}(\mathbf{x}_F|\boldsymbol{\chi}, z_1, \tau)}^{\text{coda}} \\ & \times \underbrace{(v_z(\boldsymbol{\chi}, z_1, t - \tau) + v_z(\boldsymbol{\chi}, z_1, -t - \tau))}_{\text{data}}. \end{aligned} \quad (32)$$

By setting the adaptive filters at  $a_1(\mathbf{x}_F, t) = a_2(\mathbf{x}_F, t) = \delta(t)$ , Eq. (29) is equivalent to the inverse Fourier transform of Eq. (28), where the series are truncated after  $k=2$ . Because of this truncation, and the imperfections when the method is applied in practice, this filter setting is not optimal. Instead, we may choose filters that minimize the overall energy when the terms in the right-hand side of Eq. (29) are summed. Here, we assume that the PA signals and the artifacts are not or only weakly interfering, such that the removal of events decreases the norm of the traces. This type of adaptive filters is often applied in seismic data processing<sup>39,40</sup> to overcome the limitations of inaccurate amplitudes, due to the many factors that have been outlined earlier in this section. To find the filters, we aim to solve the following minimization problem:

$$\begin{aligned} \underset{a_1, a_2}{\text{minimize}} \quad & |\widehat{I}_0(\mathbf{x}_F, t) + a_1(\mathbf{x}_F, t) * \widehat{I}_1(\mathbf{x}_F, t) \\ & + a_2(\mathbf{x}_F, t) * \widehat{I}_2(\mathbf{x}_F, t)|_n, \end{aligned} \quad (33)$$

where  $n$  indicates the norm that should be minimized. Apart from the most conventional applications, which are based on the  $\ell_2$ -norm,<sup>39</sup> various studies in the geophysical literature have been devoted to the minimization of  $\ell_1$  and other norms.<sup>40</sup> Note that  $a_1(\mathbf{x}_F, t)$  and  $a_2(\mathbf{x}_F, t)$  can be chosen space- and time-dependent. To facilitate this dependence without offering too much freedom to the filters, it is common to make use of sliding windows or non-stationary regression.<sup>41</sup> Although the filters that are required for optimal implementation of Eq. (29) are intrinsically non-stationary, we have decided to parametrize the required filters as depth- and time-independent scalars  $a_1$  and  $a_2$ , which are found by solving Eq. (33) for  $n=2$ .

Now, we demonstrate the adaptive procedure, using the 1D synthetic experiment that was introduced before. For this purpose, we compute  $\widehat{I}_0(z, t)$  by Eq. (30) and we evaluate the result at  $t=0$ . This leads to the PA image in Fig. 9(a), which is equivalent to the image that was obtained by backpropagation with a Green's function in the homogeneous model, as shown in Fig. 2(a) (scaled by a factor 2). The arrows in Fig. 8(a) indicate several artifacts in the PA image, which originate from (single and multiple) scattering. To eliminate these artifacts, the terms  $\widehat{I}_1(z, t)$  and  $\widehat{I}_2(z, t)$  can be computed by Eqs. (31) and (32). By evaluating these terms at  $t=0$  and solving the minimization problem in Eq. (33) to find scalars  $a_1$  and  $a_2$ , we find the scaled updates  $a_1\widehat{I}_1(z, t=0)$  and  $a_2\widehat{I}_2(z, t=0)$  that are given in Figs. 8(b) and 8(c). In Fig. 9(d), we show the result of adding these updates to the initial PA image  $\widehat{I}_0(z, t)$ . Note that the artifacts that were present in Fig. 9(a) have been largely suppressed. It can be observed that this is mainly caused by adding the first update  $a_1\widehat{I}_1(z, t=0)$  (rather than the second update) to the initial image  $\widehat{I}_0(z, t=0)$ . We can also observe that the first update produces additional artifacts, such as the one that is indicated by the middle arrow in Fig. 9(b). This artifact is suppressed by adding  $a_2\widehat{I}_2(z, t=0)$ , as illustrated by the arrow in Fig. 9(c). Hence, even in this simple example, both terms  $\widehat{I}_1$  and  $\widehat{I}_2$  are required to obtain adequate results. Although this

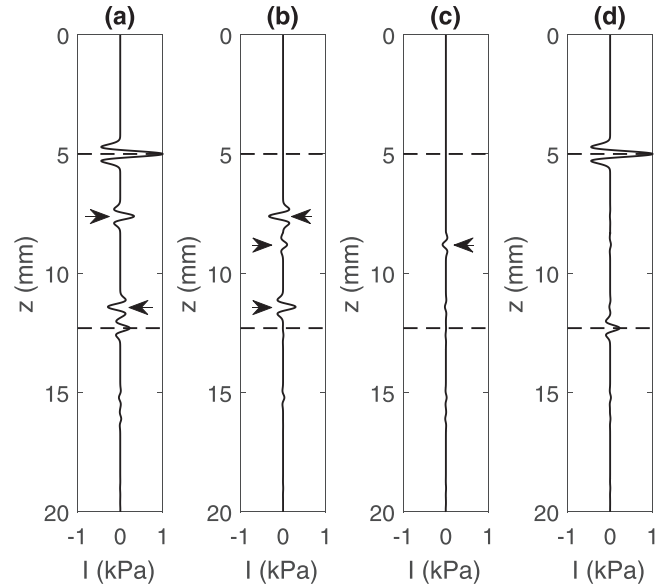


FIG. 9. (a) Contribution of the initial focusing function to the PA image  $\widehat{I}_0(z, t=0)$ . (b) Contribution of the first coda update to the PA image  $\widehat{I}_1(z, t=0)$ . (c) Contribution of the second coda update to the PA image  $\widehat{I}_2(z, t=0)$ . We have scaled the data in (b) and (c) by time- and depth-independent scalars  $a_1$  and  $a_2$ , respectively, which have been found by solving the minimization problem in Eq. (33) (where the convolutional filters have been replaced by scalars). (d) PA image after (b) and (c) have been added to (a). Particular artifacts have been indicated by arrows. Dashed lines indicate the true PA locations.

procedure allowed us to remove the most significant sources of scattering, some artifact remnants remain in Fig. 9(d). This is likely to be improved by the use of non-stationary matching filters.<sup>41</sup>

## X. STRENGTH AND LIMITATIONS

To understand the methodology that was presented in this paper at a more intuitive level, we have drawn several cartoons in Fig. 10. In Fig. 10(a), we show a typical artifact that arises when a PA source is located above a medium perturbation. When a scattered event in the data  $v_z(t)$  (having a positive traveltime) is convolved with the initial focusing function  $\widehat{f}_{2d}$  (having a negative traveltime), the traveltime along their common path is eliminated,<sup>26</sup> leaving an artifact in the image. In Fig. 10(b), we show how this artifact is being predicted by the convolution of the time-reversed direct wave from the PA source which is present in  $v_z(-t)$  with the initial focusing function  $\widehat{f}_{2d}$  and the reflection operator  $\mathcal{R}$ . This is one of the main updates that is produced by Eq. (31). Because this update has an opposite polarity compared to the event in 9 a, both events cancel each other when  $\widehat{I}_0$  and  $\widehat{I}_1$  are summed. Note that the same principle is also utilized in PAFUSion, where  $\widehat{f}_{2d}$  resembles backpropagation in the reference medium,  $\mathcal{R}$  the convolution with the reflection response and  $v_z(-t)$  can be seen as the time-gated PA data. However, while PAFUSion requires us to isolate the direct waves in  $v_z(-t)$  by removing the scattered components, such a separation is not required by our methodology. Since there is no time gate applied by our method (other than for the construction of window operator  $\Theta$ ), the scattered components of  $v_z(-t)$  create additional artifacts when Eq. (31) is

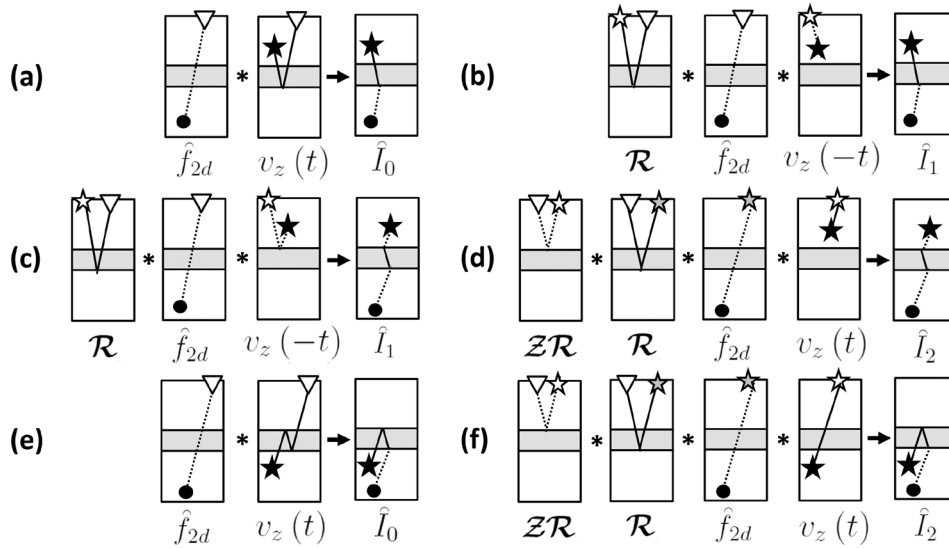


FIG. 10. (a) Emergence of an artifact in the initial image  $\hat{I}_0$  at the location of the black dot, in case that a source (black star) is located above a medium perturbation (gray layer). (b) Construction of an event  $\hat{I}_1$  that is supposed to remove the artifact in (a). (c) Emergence of an artifact in the update  $\hat{I}_1$  at the location of the black dot. (d) Construction of an event in  $\hat{I}_2$  that is supposed to remove the artifact in (c). (e) Same as (a), in case that a source is located below the medium perturbation. (f) Construction of an event in  $\hat{I}_2$  that is supposed to remove the artifact in (e). Solid lines represent raypaths along which waves propagate forward in time and dashed lines represent raypaths along which waves propagate backwards in time. White and gray stars are sources at the surface  $\partial V_1$ . White and gray triangles are receivers at this surface.

evaluated, which do not exist in PAFUSion. An example of such an artifact is indicated by the middle arrow in Fig. 9(b). The origin of this event is illustrated in Fig. 10(c). To eliminate this artifact, the update of  $\hat{I}_2$  should be added to the image. As shown by the arrow in Fig. 9(c), the new update does indeed contain an event at the desired travelttime with an opposite polarity. As explained by the cartoon in Fig. 10(d), this event originates from the convolution of reflections in  $\mathcal{Z}\mathcal{R}$ , reflections in  $\mathcal{R}$ , the initial focusing function  $\hat{f}_{2d}$  and  $v_z(t)$ , at the moment that Eq. (32) is evaluated.

Unlike PAFUSion, the proposed methodology is also valid in cases where PA sources are located below or in between medium perturbations. In Fig. 10(e), we illustrate the generation of a particular artifact from a deep PA source. The sequence of operations that is applied in Eq. (32) results in the construction of a similar event with opposite polarity during the construction of  $\hat{I}_2$ , see Fig. 10(f). Hence, this artifact is suppressed when  $\hat{I}_0$  and  $\hat{I}_2$  are summed. We can demonstrate this situation with a modified synthetic example, where an additional density perturbation has been added to the model that was presented earlier in the paper, see Fig. 11(a). We have implemented PAFUSion by isolating the direct wave from the upper PA source and crosscorrelating the result with the reflection response. In this process, we have compensated for the transmission losses of direct wave propagation through the upper density perturbation to achieve an optimal result. Although this procedure allowed us to obtain a reasonable PA image, as shown in Fig. 11(b), various artifacts have emerged from the presence of the shallow density perturbation that has been added to the model. When the ISP is solved by Eq. (28), however, a perfect image is obtained, see Fig. 11(c). Finally, it should be mentioned that the adaptive strategy that was proposed in Eq. (29) proved insufficient to obtain a similar result, as shown in Fig. 11(d). Although the improvements over the

PAFUSion image are clear, because perturbations above the PA source have been taken into account, some smaller artifacts remain present in the adaptive result. This can be circumvented either by including higher-order updates or by using non-stationary adaptive filters.<sup>41</sup>

Although the procedure that is described in this paper requires a model of the propagation velocity, the solutions of the multidimensional Marchenko equation are remarkably

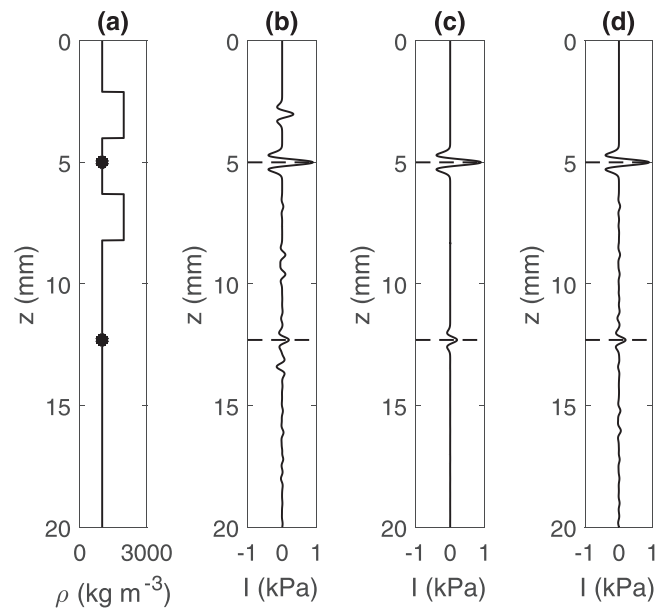


FIG. 11. (a) Modified density model with similar properties as the model in Fig. 2(a), with an additional shallow density perturbation added above the upper PA source. (b) PA image as retrieved by PAFUSion for this model. (c) PA image as retrieved by Eq. (28) (where the series have been truncated after 10 terms), representing single-sided wavefield focusing without adaptive subtraction. (d) Same, for single-sided wavefield focusing (truncated after two terms) with adaptive subtraction, using Eq. (29).

robust with respect to errors in such a model, which has been validated by several studies.<sup>25,38,42</sup> Apart from the obvious misplacement of the target signals and spatial blurring in 2D/3D applications, the predicted artifacts are still internally consistent, which can be useful for structural imaging. To illustrate this feature of the proposed methodology, we generated another PA image, using the model in Fig. 11(a). This time, however, we have computed the initial focusing function in an erroneous model with an overestimated velocity of  $c = 2000$  m/s rather than the correct  $c = 1500$  m/s, which has been used before. The result is shown in Fig. 12(a). Although the retrieved PA signals are positioned too deep in this case, the artifacts have all been removed, validating the robustness of the methodology with respect to velocity errors. To illustrate that the methodology can be applied with perturbations in the velocity model as well as in the density model, we repeat PA imaging in a medium with both velocity and density perturbations. We use the density model in Fig. 11(a) and the velocity model in Fig. 12(b). In Fig. 12(c), we demonstrate that a perfect PA image can be constructed in this case, if we use the exact velocity model for backpropagation. In Fig. 12(d), we show an equivalent result, where we used a homogeneous velocity model (with  $c = 2000$  m/s) for backpropagation instead. It is observed once again that the artifacts of reflections have been suppressed well, but that the PA signals have been positioned too shallow, which can be attributed to the erroneous velocities that we used for backpropagation. We also note that the amplitudes of the PA signals are underestimated. This can be explained by the fact that transmission effects have not been taken into account.

As we remarked earlier, the wavelet of the PA data should be zero phase. To demonstrate this, we repeat the PA imaging exercise of Fig. 11(c) [using the density model in

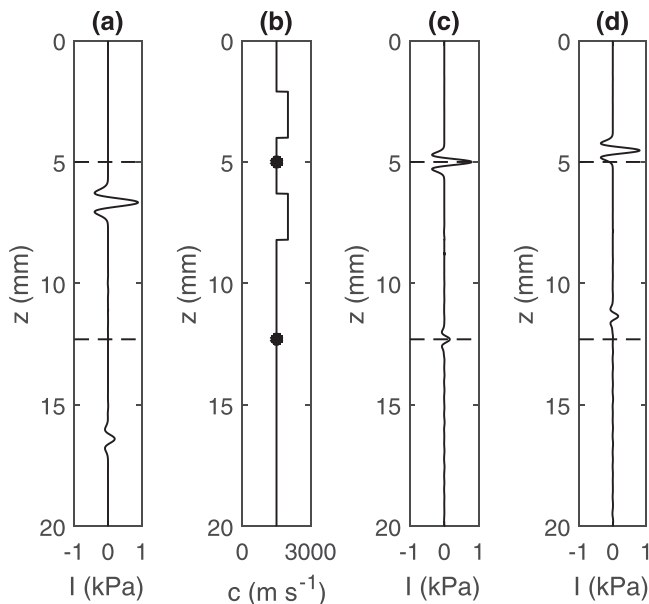


FIG. 12. (a) PA image, obtained in a homogeneous model with velocity  $c = 2000$  m/s. (b) Modified velocity model, which includes perturbations. (c) PA image obtained from the model in (b) by single-sided focusing, obtained in the correct velocity model. Same as (d), obtained in a homogeneous velocity model with  $c = 1500$  m/s.

Fig. 11(a) and a constant velocity model with  $c = 1500$  m/s], but we phase-rotated the PA data prior to imaging by multiplication with  $\exp(j\pi/2)$ . The result is shown in Fig. 13(a). Since the predicted updates are out of phase with the observed artifacts in the backpropagated data, the subtraction process is not successful in this case. Since adaptive filters can correct for the phase error, this problem can be overcome by using the adaptive strategy that was proposed in Sec. IX. This is illustrated in Fig. 13(b). Note that the retrieved events have a different phase compared to Fig. 11(c). This is because the induced phase rotation is included in the PA signals and therefore in their reconstruction. Unlike in Fig. 13(a), the artifacts from reflections have been suppressed well in Fig. 13(b). In order to achieve this, we have used least-squares filters of 11 samples.<sup>39</sup>

We would like to add a remark on the resolution of the proposed solution. As indicated before, limitations are posed by the duration of the source pulse, restricting  $t_w$  which is used for the design of truncation operator  $\Theta$ . In our examples,  $t_w = 0.5 \mu\text{s}$ , as we have mentioned earlier. Any reflection at  $t \leq 2 * t_w = 1.0 \mu\text{s}$  after the direct wavefield will interfere with the direct wavefield. Consequently, it cannot be processed correctly by the current implementation of the methodology. To demonstrate this phenomenon, we placed a density perturbation at  $\Delta z = 0.60$  mm below the upper PA source, as indicated in Fig. 13(c). In this modified model, the first reflection arrives at  $t = 2\Delta z/c = 0.8 \mu\text{s}$  ( $< 1.0 \mu\text{s}$ ) after the direct wave and, consequently, these waves start to interfere. As a result of this inevitable interference, a weak artifact will emerge in the result, as indicated by the arrow in Fig. 13(d). When the PA source is placed even closer to the density perturbation, this artifact will get more pronounced, as it cannot be processed correctly, and in the limit  $\Delta z \rightarrow 0$  the event cannot be removed at all. For similar reasons,

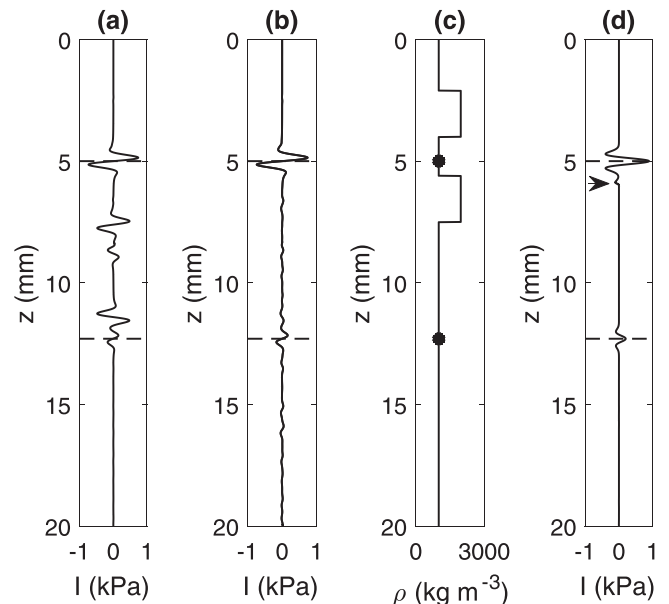


FIG. 13. (a) PA image of phase-rotated PA data. (b) Adaptive PA image of the phase-rotated data. (c) Density model, where the density perturbation is placed  $\Delta z = 0.60$  mm below the upper PA source. (d) PA image obtained from the model in (c) by single-sided focusing. The arrow points to an artifact.

complete elimination of multiple reflections from layers or contrasts with thicknesses that exceed  $c * t_w = 0.75$  mm is not possible, given the frequency band of the recorded reflection response. These limitations of the Marchenko equation have been well documented in the existing literature.<sup>24</sup>

In all examples of this paper, we have restricted ourselves to 1D simulations. The multidimensional Marchenko equation, however, can also be evaluated in 2D and 3D under the restriction of smoothly curved interfaces.<sup>23</sup> While sharp discontinuities, such as point diffractors, break some of the assumptions that are made in the underlying derivation,<sup>26</sup> approximate solutions can still be found, even in complicated media with many diffractors.<sup>43</sup> To solve the ISP in 2D or 3D, the multidimensional Marchenko equation should be evaluated at each image point in the computational domain  $\mathcal{D}$ , which can increase the computational cost. To reduce this cost to some extent, it can be beneficial for  $\mathcal{D}$  to be a small subset of the total volume  $\mathcal{V}$  only. We are currently working on the implementation of PA imaging in 2D and hope to report on that in the future.

## XI. CONCLUSION

We have derived a solution for acoustic inverse source problems from the multidimensional Marchenko equation. The solution can be used to determine the distribution of simultaneously acting sources from a set of observations. Unlike the conventional solutions from time-reversed acoustics, observations are only required at a single, open boundary. The method uses backpropagation of the acquired data in a reference medium, plus a series of subsequent updates to remove the artifacts that are created during this process, because of (single and multiple) scattering. The methodology can be interpreted as a generalization of the PAFUSion concept, that was recently derived for photoacoustic imaging, based on intuitive reasoning. If accurate reflection data are available over a broad frequency band, straightforward implementation provides a solution to the inverse source problem, even in heterogeneous models. However, limitations are posed by the finite frequency band of the data, which is controlled by the duration of the pulse that is used to obtain the reflection response. Scattering effects with a period less than the pulse duration ( $2 * t_w$ ) will interfere with the direct wavefield and consequently, these effects cannot be removed. Since the mechanism by which the scattering artifacts are predicted is independent on velocity information, the method is remarkably robust with respect to errors in the model of the propagation velocity. The presence of such errors will stretch (and blur) the reconstructed images in space, but do not result in additional artifacts. The methodology is very sensitive to the amplitude of the reflection response. Since correct amplitudes are often difficult to record in practice, we have presented an alternative solution that is based on adaptive subtraction. Unlike the previous approach, this solution is not exact and requires that target PA signals and scattering contributions do not overlap or overlap only weakly, such that adaptive filters can be found by minimizing the energy norm of the obtained images. Although the most successful filters are likely to be time-

and/or depth-dependent and should consist of multiple parameters, we have shown that a significant attenuation of scattering artifacts can also be achieved if we parametrize these filters as time- and depth-independent scalars.

## ACKNOWLEDGMENTS

This research is financially supported by the Nederlandse Organisatie voor Wetenschappelijk Onderzoek (NWO), domein Toegepaste Technische Wetenschappen (STW / TTW) (Grant No. VENI.13078). We thank Jan Thorbecke, Myrna Staring, Lele Zhang, Joeri Brackenhoff, Chris Reinicke (Delft University of Technology), Niels Grobbe (Massachusetts Institute of Technology), Matteo Ravasi (Statoil Bergen), Sjoerd de Ridder, Giovanni Meles, Andrew Curtis, Carlos Alberto da Costa Filho, Katrin Löer (University of Edinburgh), Marcin Dukalski, Koos de Vos (Shell E&P), Ivan Vasconcelos (Utrecht University) and Yi Liu (Norwegian University of Science and Technology Trondheim) for various discussions that have contributed to this work.

<sup>1</sup>G. A. McMechan, J. H. Luetgert, and W. D. Mooney, "Imaging of earthquake sources in Long Valley Caldera, California, 1983," *Bull. Seismol. Soc. Am.* **75**(4), 1005–1020 (1985).

<sup>2</sup>C. Larmat, J. P. Montagner, M. Fink, Y. Capdeville, A. Tourin, and E. Clévéde, "Time-reversal imaging of seismic sources and application to the great Sumatra earthquake," *Geophys. Res. Lett.* **33**(19), L19312, doi:10.1029/2006GL026336 (2006).

<sup>3</sup>F. Song and M. N. Toksöz, "Full-waveform based complete moment tensor inversion and source parameter estimation from downhole microseismic data for hydrofracture monitoring," *Geophysics* **76**(6), WC103–WC116 (2011).

<sup>4</sup>Z. Li and M. van der Baan, "Microseismic event localization by acoustic time reversal extrapolation," *Geophysics* **81**(3), KS123–KS134 (2016).

<sup>5</sup>L. Eisner, S. Williams-Stroud, A. Hill, P. Duncan, and M. Thornton, "Beyond the dots in the box: Microseismicity-constrained fracture models for reservoir simulation," *Leading Edge* **29**(3), 326–333 (2010).

<sup>6</sup>W. A. Kuperman, W. S. Hodgkiss, H. C. Song, T. Akal, C. Ferla, and D. R. Jackson, "Phase conjugation in the ocean: Experimental demonstration of an acoustic time-reversal mirror," *J. Acoust. Soc. Am.* **103**(1), 25–40 (1998).

<sup>7</sup>E. H. Saenger, G. K. Kocur, R. Jud, and M. Torrilhon, "Application of time reverse modeling on ultrasonic non-destructive testing of concrete," *Appl. Math. Modell.* **35**(2), 807–816 (2011).

<sup>8</sup>L. V. Wang and S. Hu, "Photoacoustic tomography: In vivo imaging from organelles to organs," *Science* **335**(6075), 1458–1462 (2012).

<sup>9</sup>P. Beard, "Biomedical photoacoustic imaging," *Interface Focus* **1**(4), 602–631 (2011).

<sup>10</sup>S. A. Ermilov, T. Khampirad, A. Conjusteau, M. H. Leonard, R. Laceywell, K. Mehta, T. Miller, and A. A. Oraevsky, "Laser optoacoustic imaging systems for detection of breast cancer," *J. Biomed. Opt.* **14**(2), 024007 (2009).

<sup>11</sup>D. R. Bauer, R. Olafsson, L. G. Montilla, and R. S. Witte, "3-D photoacoustic and pulse echo imaging of prostate tumor progression in the mouse window chamber," *J. Biomed. Opt.* **16**(2), 026012 (2011).

<sup>12</sup>Y. Xu and L. V. Wang, "Time reversal and its application to tomography with diffracting sources," *Phys. Rev. Lett.* **92**(3), 033902 (2004).

<sup>13</sup>D. Gajewski and E. Tessmer, "Reverse modelling for seismic event characterization," *Geophys. J. Int.* **163**(1), 276–284 (2005).

<sup>14</sup>B. Artman, I. Podlatchikov, and B. Witten, "Source location using time-reverse imaging," *Geophys. Prospect.* **58**(5), 861–873 (2010).

<sup>15</sup>M. Fink, "Time reversed acoustics," *Phys. Today* **50**(3), 34–40 (1997).

<sup>16</sup>M. Fink and C. Prada, "Acoustic time-reversal mirrors," *Inverse Probl.* **17**(1), R1–R38 (2001).

<sup>17</sup>K. Wapenaar, J. Fokkema, and R. Snieder, "Retrieving the Green's function in an open system by cross-correlation: A comparison of approaches," *J. Acoust. Soc. Am.* **118**(5), 2783–2786 (2005).

<sup>18</sup>J. F. Aubry, M. Tanter, J. Gerber, J. L. Thomas, and M. Fink, "Optimal focusing by spatio-temporal inverse filter: II. Experiments. Application to

- focusing through absorbing and reverberating media,” *J. Acoust. Soc. Am.* **110**(1), 48–58 (2001).
- <sup>19</sup>G. Paltauf, J. A. Viator, S. A. Prael, and S. L. Jacques, “Iterative reconstruction algorithm for optoacoustic imaging,” *J. Acoust. Soc. Am.* **112**(4), 1536–1544 (2002).
- <sup>20</sup>F. Bargazani and R. Snieder, “Optimal source imaging in elastic media,” *Geophys. J. Int.* **204**(1), 1134–1147 (2016).
- <sup>21</sup>M. K. A. Singh and W. Steenbergen, “Photoacoustic-guided focused ultrasound (PAFUSion) for identifying reflection artifacts in photoacoustic imaging,” *Photoacoustics* **3**(4), 123–131 (2015).
- <sup>22</sup>M. K. A. Singh, M. Jaeger, M. Frenz, and W. Steenbergen, “*In vivo* demonstration of reflection artifact reduction in photoacoustic imaging using synthetic aperture photoacoustic-guided focused ultrasound (PAFUSion),” *Biomed. Opt. Exp.* **7**(8), 2955–2972 (2016).
- <sup>23</sup>K. Wapenaar, J. Thorbecke, J. van der Neut, F. Broggin, E. Slob, and R. Snieder, “Green’s function retrieval from reflection data, in absence of a receiver at the virtual source position,” *J. Acoust. Soc. Am.* **135**(5), 2847–2861 (2014).
- <sup>24</sup>E. Slob, K. Wapenaar, F. Broggin, and R. Snieder, “Seismic reflector imaging using internal multiples with Marchenko-type equations,” *Geophysics* **79**(2), S63–S76 (2014).
- <sup>25</sup>F. Broggin, R. Snieder, and K. Wapenaar, “Data-driven wave field focusing and imaging with multidimensional deconvolution: Numerical examples for reflection data with internal multiples,” *Geophysics* **79**(3), WA107–WA115 (2014).
- <sup>26</sup>J. van der Neut, I. Vasconcelos, and K. Wapenaar, “On Green’s function retrieval by iterative substitution of the coupled Marchenko equations,” *Geophys. J. Int.* **203**(1), 792–813 (2015).
- <sup>27</sup>R. Burridge, “The Gelfand-Levitan, the Marchenko and the Gopinath-Sondhi integral equations of inverse scattering theory, regarded in the context of inverse impulse-response problems,” *Wave Motion* **2**(4), 305–323 (1980).
- <sup>28</sup>J. H. Rose, “Single-sided autofocusing of sound in layered media,” *Inverse Probl.* **18**(6), 1923–1934 (2002).
- <sup>29</sup>S. Singh, R. Snieder, J. van der Neut, J. Thorbecke, E. Slob, and K. Wapenaar, “Accounting for free-surface multiples in Marchenko imaging,” *Geophysics* **82**(1), R19–R30 (2017).
- <sup>30</sup>J. T. Fokkema and P. M. van den Berg, *Seismic Applications of Acoustic Reciprocity* (Elsevier Science, New York, 1993).
- <sup>31</sup>C. P. A. Wapenaar, “Reciprocity theorems for two-way and one-way wave vectors: A comparison,” *J. Acoust. Soc. Am.* **100**(6), 3508–3518 (1996).
- <sup>32</sup>N. N. Bojarski, “Generalized reaction principles and reciprocity theorems for the wave equations, and the relationship between the time-advanced and time-retarded fields,” *J. Acoust. Soc. Am.* **74**(1), 281–285 (1983).
- <sup>33</sup>J. Laufer, D. Delpy, C. Elwell, and P. Beard, “Quantitative spatially resolved measurement of tissue chromophore concentrations using photoacoustic spectroscopy: Application to the measurement of blood oxygenation and haemoglobin concentration,” *Phys. Med. Biol.* **52**(1), 141–168 (2007).
- <sup>34</sup>K. Wapenaar, J. van der Neut, and E. Slob, “Unified double- and single-sided homogeneous Green’s function representations,” *Proc. R. Soc. A* **472**(2190), 20160162 (2016).
- <sup>35</sup>J. van der Neut, K. Wapenaar, and E. Slob, “Marchenko imaging below complex overburdens in the Middle East,” in *SEG/KOC Workshop, Seismic Multiples—Are They Signal or Noise?* (2014).
- <sup>36</sup>J. Brackenhoff, “Rescaling of incorrect source strength using Marchenko redatuming,” M.Sc. thesis, Delft University of Technology, Delft, the Netherlands (2016).
- <sup>37</sup>M. Ravasi, I. Vasconcelos, A. Kritski, A. Curtis, C. A. da Costa Filho, and G. A. Meles, “Target-oriented Marchenko imaging of a North Sea field,” *Geophys. J. Int.* **205**(1), 99–104 (2016).
- <sup>38</sup>J. van der Neut and K. Wapenaar, “Adaptive overburden elimination with the multidimensional Marchenko equation,” *Geophysics* **81**(5), T265–T284 (2016).
- <sup>39</sup>D. J. Verschuur, A. J. Berkhou, and C. P. A. Wapenaar, “Adaptive surface-related multiple elimination,” *Geophysics* **57**(9), 1166–1177 (1992).
- <sup>40</sup>Y. M. Batany, L. T. Duarte, D. Donno, J. M. T. Romano, and H. Chauris, “Adaptive multiple subtraction: Unification and comparison of matching filters based on the  $l_q$ -norm and statistical dependence,” *Geophysics* **81**(1), V43–V54 (2016).
- <sup>41</sup>S. Fomel, “Adaptive multiple subtraction using regularized nonstationary regression,” *Geophysics* **74**(1), V25–V33 (2009).
- <sup>42</sup>G. Meles, K. Lör, M. Ravasi, A. Curtis, and C. A. da Costa Filho, “Internal multiple prediction and removal using Marchenko autofocusing and seismic interferometry,” *Geophysics* **80**(1), A7–A11 (2015).
- <sup>43</sup>K. Wapenaar, J. Thorbecke, J. van der Neut, I. Vasconcelos, and E. Slob, “Marchenko imaging below an overburden with random scatterers,” in *EAGE Extended Abstracts*, Th-E102-10 (2014).